iScience

Article

Bioelectric characterization of senescing human keratinocytes

Graphical abstract

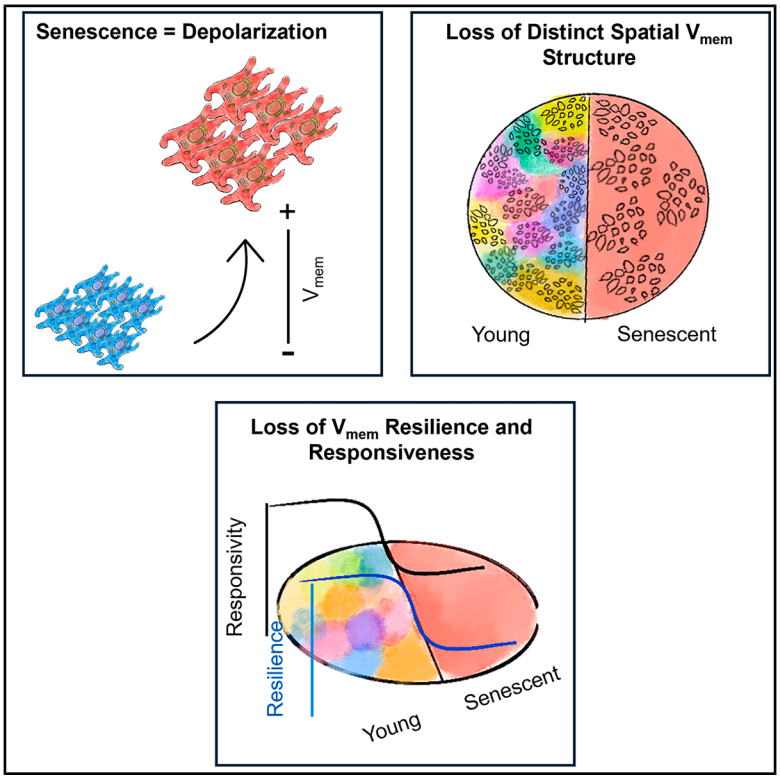

Authors

Hamid Sediqi, Michael Levin

Correspondence

michael.levin@tufts.edu

In brief

Biological sciences; Biotechnology; Bioengineering

Highlights

- Senescence is marked by depolarization of keratinocyte V_{mem}
- Bioelectric modulation shapes SASP cytokine expression during senescence
- Senescent cells show reduced bioelectric resilience and responsiveness
- Loss of spatial V_{mem} structure emerges in late-stage keratinocyte cultures

Sediqi & Levin, 2025, iScience *28*, 113275
September 19, 2025
https://doi.org/10.1016/j.isci.2025.113275

CellPress

iScience

CellPress
OPEN ACCESS

Article

Bioelectric characterization of senescing human keratinocytes

Hamid Sediqi[1] and Michael Levin[1,2,3,*]
[1]Allen Discovery Center at Tufts University, Medford, MA 02155, USA
[2]Wyss Institute for Biologically Inspired Engineering, Harvard University, Boston, MA 02115, USA
[3]Lead contact
*Correspondence: michael.levin@tufts.edu
https://doi.org/10.1016/j.isci.2025.113275

SUMMARY

Aging disrupts tissue integrity through the accumulation of senescent cells that impair morphology, signaling, and regeneration. We investigated how bioelectric signaling, specifically resting membrane potential (V_{mem}), guides the transition to senescence in human keratinocytes. Using voltage-sensitive dyes, we tracked V_{mem} alongside senescence markers, chromatin state, and senescence-associated secretory phenotype (SASP) cytokines. Senescence was marked by depolarization, increased inter-culture heterogeneity, reduced intra-culture variability, and loss of spatial V_{mem} organization. SASP activation was partial: depolarization selectively enhanced interleukin-6 (IL-6) but not IL-1α or IL-8, indicating V_{mem} shapes the senescent secretome. Senescent cells showed reduced responsiveness to hyperpolarizing drug pinacidil and impaired bioelectric resilience. Hyperpolarization attenuated, and depolarization exacerbated, senescence-associated phenotypes. These findings support the morphostatic information loss theory, which posits that aging results from breakdown of bioelectrically encoded cues that preserve tissue structure. V_{mem} emerges as a low-dimensional integrator of cell state and spatial order, offering a biophysical target to delay senescence and maintain tissue coordination.

INTRODUCTION

Aging, the progressive decline of form and function, affects almost all multicellular organisms.[1,2] Many theories have been proposed to explain the cause of aging and generally fall into two broad categories: damage-based and programmatic-based. Damage-based theories argue that aging occurs due to the accumulation of damage caused by oxidative stress, DNA damage, and the progressive malfunction of cellular repair mechanisms.[3,4] Conversely, programmatic-based theories posit that aging is hardwired into the genome to give an evolutionary benefit at the cost of a limited lifespan.[5,6] Despite much effort consistent with these hypotheses, there is a notable lack of definitive anti-aging treatments.[7] This led to the emergence of the information-loss theory of aging which posits that aging is caused due to the progressive loss of biological information required to maintain homeostasis.[8] This loss of information is said to occur at the level of the epigenome—changes in the methylation profiles lead to epigenetic drift, reducing the fidelity of information driving cellular processes, and causing loss of cell identity.[8]

Theories of aging focused on loss of information at the genetic (telomere) or epigenetic levels can explain changes in cellular properties. However, resistance to aging is a whole-body phenomenon that is likely connected to the overall processes of embryogenesis and regeneration. Resistance to aging is not something that is only needed later in life—it is likely part of the general machinery needed for a body to maintain order amidst the daily replacement of cells and the molecular noise that constantly threaten to disrupt tissue- and organ-level structures.[9,10] Aging can be seen as the eventual failure of fundamental, ubiquitous mechanisms that organize cellular and molecular events toward the maintenance and repair of the target morphology and away from degeneration and cancer.[11–13]

One possible cause of aging is progressive loss of morphostatic information.[2] During development, cellular collectives traverse the anatomical morphospace (the latent space of potential geometric configurations), to reach their target morphology—a region within that space that corresponds to the correct anatomy of a given species.[14,15] Importantly, even after development into an adult, maintaining the final adult morphology is a highly active state that must counteract environmental stress and noise. It is likely that the key to longevity is understanding the computational processes enabling cellular collectives to establish and maintain order at various scales. What maintains the information needed for continuous upkeep of structure, within a specific region of morphospace over decades? A number of mechanisms have been implicated in on-going morphostasis, including dynamic biochemical and biomechanical gradients. Here, we focus on endogenous bioelectricity: an important modality that has been implicated in large-scale morphogenetic control in embryogenesis, regeneration, and cancer suppression.[16–18]

Endogenous bioelectrical signaling is driven by ion channels and pumps, present in all cells—not only neurons. The resting potential of cells regulates proliferation, migration, differentiation, and gene expression.[19–28] However, as in the brain, bioelectric signaling is not just a factor determining single cell behavior: due to electrical synapses known as gap junctions[29] and large-scale trans-epithelial electric fields,[30,31] tissue-level bioelectric states propagate and integrate across considerable distances *in vivo*. Spatial patterns of resting membrane potential have been shown to regulate the morphogenesis of the wing, eye, heart, limb, and brain in a range of model species and human patients (reviewed in[16–18,32,33]), and it is becoming clear that bioelectric regionalization provides an important underlying scaffold for defining tissue boundaries and organ-level structure.[34] Recent work has especially shown that a number of birth defects, induced both chemically and genetically, exert their teratogenic influence by blurring the endogenous bioelectric prepatterns that set the size and shape of the brain; moreover, the sharpness of these patterns are an attractive target for therapeutics because reinforcing the crisp boundaries between different bioelectric regions results in repair of severe defects of the brain, gut, and heart.[35–38] Interestingly, cancer—another loss of tissue-level order, which a human intact body must battle for decades[9,39]—can likewise be induced by disruptions of endogenous bioelectric states and normalized by therapeutic restoration of V_{mem} and gap junctional connectivity.[40–45]

While much work on V_{mem} patterns has occurred in various model systems,[46,47] less is known about human cells—a prerequisite for developing therapeutics. More generally, while resting potential of human cells, such as mesenchymal stem cells in culture,[48–54] has been studied, it is not known what kind of multicellular patterns would exist *in vitro*—a scenario different from the cells' usual evolutionarily established organ context, in which embryonic organizer processes are not available to regionalize V_{mem} patterns. Finally, the changes in bioelectric pattern over long timescales, beyond embryogenesis, are not well characterized. Thus, here, we sought to address these knowledge gaps by studying bioelectric states in human cells *in vitro*, during their natural process of senescence, using a state-of-the-art voltage dye visualization method that goes beyond first-generation bioelectric profiling methods.[55,56]

While there is a paucity of research into the role of bioelectricity in aging, some researchers have investigated ion channels and membrane potential changes in senescing cells. Plasma membrane depolarization has been suggested to be an important trigger for the induction of senescence,[57–59] via depolarization as a result of increased expression of voltage-gated sodium channels.[58,59] Knocking down these channels prevented the expression of p53 and the downregulation of mitotic genes.[59] Experiments exposing cells to depolarizing treatments were shown to induce senescence.[58,59] Together with the functional evidence for a role of bioelectric patterns in regenerative, embryonic, and neoplastic contexts,[60,61] these data suggest the importance of bioelectricity not only as a biomarker of aging, but also reveal it to have a functional role in cellular senescence.

Thus, we proposed a model in which loss of morphostatic information is specifically due to spatial bioelectric patterns degrading with age, becoming blurred and thus making it more difficult for individual cells, even when replaced with new progeny, to take on appropriate system-level roles within the anatomical structure.[1] This model makes a number of non-mutually exclusive predictions, which we tested here: (1) Is there an absolute shift in mean V_{mem} during senescence? (2) Is there a reduction of precision (increase in variance) among cells with increasing culture duration? (3) Is there spatial order (separated domains of resting potential) which becomes less distinct over time? And (4) does cells' ability to respond to bioelectric signals[62] or resilience (time to return to equilibrium after perturbation) decline in senescence?

To explore these ideas, we used human keratinocytes isolated from the neonatal epidermis. According to the manufacturer, these cells have 15 population doubling before undergoing cell-cycle arrest.[63] Progenitor keratinocytes residing in the basal layer of the epidermis initially undergo proliferation, then differentiate while migrating toward the surface of the skin.[64] However, with increasing age, progenitor keratinocytes in the basal and spinous layer increasingly become senescent, reducing the skin's regenerative potential, thinning the epidermis, and impairing homeostasis.[65] As keratinocytes are the dominant cell type in skin, *in vitro* cultures provide researchers with a highly relevant model for studying skin aging processes such as senescence.

In this study, we investigate whether senescence alters the spatial organization, responsiveness, and resilience of the membrane potential in human epidermal keratinocytes. While membrane depolarization is a known feature of senescent cells, the broader implications of senescence for bioelectric patterning and signaling remain poorly understood. Here, we show that senescent-associated depolarization coincides with increased inter-culture heterogeneity, reduced intra-culture variability, diminished cellular responsiveness, and disrupted spatial V_{mem} organization. By experimentally modulating resting potential, we further demonstrate that hyperpolarization attenuates, while depolarization exacerbates, senescence-associated phenotypes—positioning membrane potential not just as a biomarker, but as a functional regulator of cellular aging dynamics.

RESULTS

Senescent keratinocytes exhibit depolarization, and reduced intra-culture, but increased inter-culture, V_{mem} heterogeneity

We quantified baseline bioelectrics by imaging keratinocytes cultured for varying durations and stained with 600 nM of the voltage-sensitive dye BeRST.[66–70] BeRST is comprised of a silicon rhodamine fluorophore attached to a phenylvenevinylene molecular wire that is sensitive to changes in the electric field.[55,69] The mechanism underpinning the voltage sensing involves photoinduced electron transfer (PeT). Staining cells with BeRST results in the molecular wire embedding into the plasma membrane, while the silicon rhodamine head resides on the surface. If the membrane potential is hyperpolarized the electron-rich molecular wire quenches the head, causing a reduction in fluorescence and Lifetime. Upon membrane depolarization, the PeT mechanism is disrupted, leading to an increase in fluorescence and Lifetime from the silicon rhodamine head.[66,67,69,70] This dye provides important advantages over other voltage

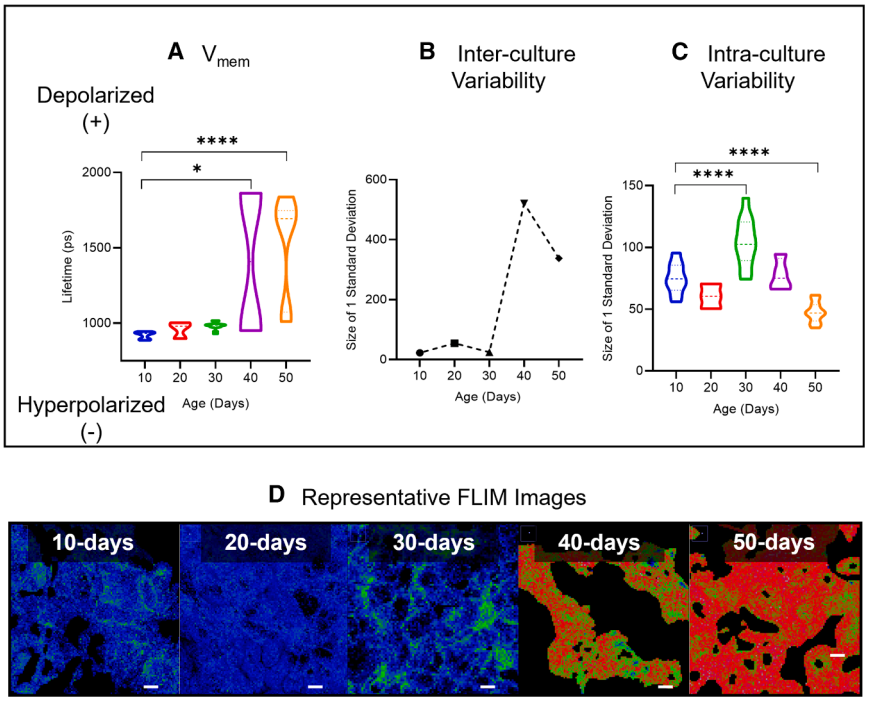

Figure 1. Human epidermal keratinocytes undergoing senescence exhibit membrane depolarization, increased inter-culture, and reduced intra-culture V_{mem} heterogeneity

Human epidermal keratinocytes were cultured onto flat-bottom 96-well plate (pre-coated with poly-L-lysine for 1 h) 24 h prior to imaging. Cells were loaded with 600 nM BeRST in keratinocyte media for 30-min in humidified incubator at 37°C and 5% CO_2, then washed twice with PBS and kept in fresh keratinocyte media for imaging with the Leica SP8 confocal microscope.

(A) Human epidermal keratinocytes became significantly depolarized at day 40 and 50 (n = 6 biological replicates, $p < 0.05$ and $p < 0.001$, respectively).

(B) The calculated standard deviation of each biological replicate shows increased variability between replicates.

(C) The average standard deviation within each biological replicate (*i.e.*, within a single dish) was calculated by averaging the standard deviation in each age group. This analysis revealed that variability within a single cell culture significantly decreases with culture duration (n = 6 biological replicates, $p < 0.05$ and $p < 0.001$, respectively).

(D) Representative FLIM images of BeRST stained keratinocytes. Violin plots (A,C) show the full data distribution for each group; the thick central dashed line represents the mean, and the upper and lower dotted lines represent the 75th and 25th percentiles, respectively. Statistical comparisons were performed using Dunn's multiple comparisons test; scale bars, 10 μm.

dyes currently being used. Firstly, it has a near-far red excitation, reducing photo-toxicity and enabling long-term live imaging. Secondly, since PeT underpins the voltage sensing mechanism of this dye—unlike other dyes that use the movement of a charged fluorophore in/out of the cell—the fluorescence intensity and Lifetime is not altered by changes in membrane permeability. This reduces artifacts introduced by differential dye uptake by cells.

Our results revealed significant depolarization of keratinocytes upon reaching day 40 ($p < 0.05$, n = 4 biological replicates) and 50 ($p < 0.05$, n = 13 biological replicates) in culture (Figure 1A) relative to day 10 cells (n = 9 biological replicates). This coincided with increased levels of three senescent markers: p16^{INK4A}[71] levels (Figure 2A), SA-β-galactosidase activity[72] (Figures 2B and 2D-i), and senescent associated heterochromatin foci (Figure 2C) as measured by the chromatin condensation parameter (CCP)[73] ($p < 0.05$, n = 4 biological replicates; $p < 0.0001$, n = 6 biological replicates; $p < 0.0001$, n = 6 biological replicates). Importantly, CCP detects edges[74,75] formed by SAHF punctate[76] as can be seen in 50-day cultures in Figures 2D-ii and 2D-iii. To confirm that 50-day cells were indeed undergoing senescence rather than quiescence, we characterized the expression of key cytokines associated with the senescence-associated secretory phenotype (SASP): interleukin-1α (IL-1α), IL-6, and IL-8 (Figure S2). RT-qPCR analysis revealed a significant increase in IL-6 mRNA levels in 50-day cultures compared to 10-day cultures ($p < 0.01$, n = 3 biological replicates), consistent with canonical SASP activation. In contrast, IL-1α and IL-8 expression showed no statistically significant change. This selective upregulation of IL-6 is consistent with context-dependent selective SASP activation, a feature observed in other models of cellular senescence.[77] It also supports the notion that the observed bioelectric and chromatin changes in 50-day cells are linked to senescence, rather than a general stress response or quiescent arrest, and are indicative of a partial SASP activation.

The degree of V_{mem} heterogeneity between biological replicate cultures increased markedly with time in culture, with standard deviation values rising over 22-fold at day 40 and 15-fold at day 50 compared to 10-day cultures (Figure 1B). In contrast, variability within individual cultures significantly declined: 50-day cultures exhibited a 38% reduction in intra-culture heterogeneity relative to 10-day cultures ($p < 0.0001$, n = 9–16 biological replicates) (Figure 1C). These opposing trends suggest that as keratinocytes remain longer in culture and begin to acquire senescent features, cells within a given dish first converge toward a shared V_{mem} distribution—prior to the bioelectric switch to depolarization—even as substantial V_{mem} variability persists across dishes. At day 40, the V_{mem} distribution across replicates is clearly bimodal, reflecting a mix of cultures in polarized and depolarized states (Figure 1A). By day 50, although some cultures remain more polarized, the overall distribution shifts toward depolarization, and intra-dish consistency remains high. These findings suggest that membrane potential serves not only as a sensitive indicator of senescence but also as a reproducible feature that captures the internal bioelectric uniformity of individual microenvironments, despite broader variability in senescence onset across cultures.

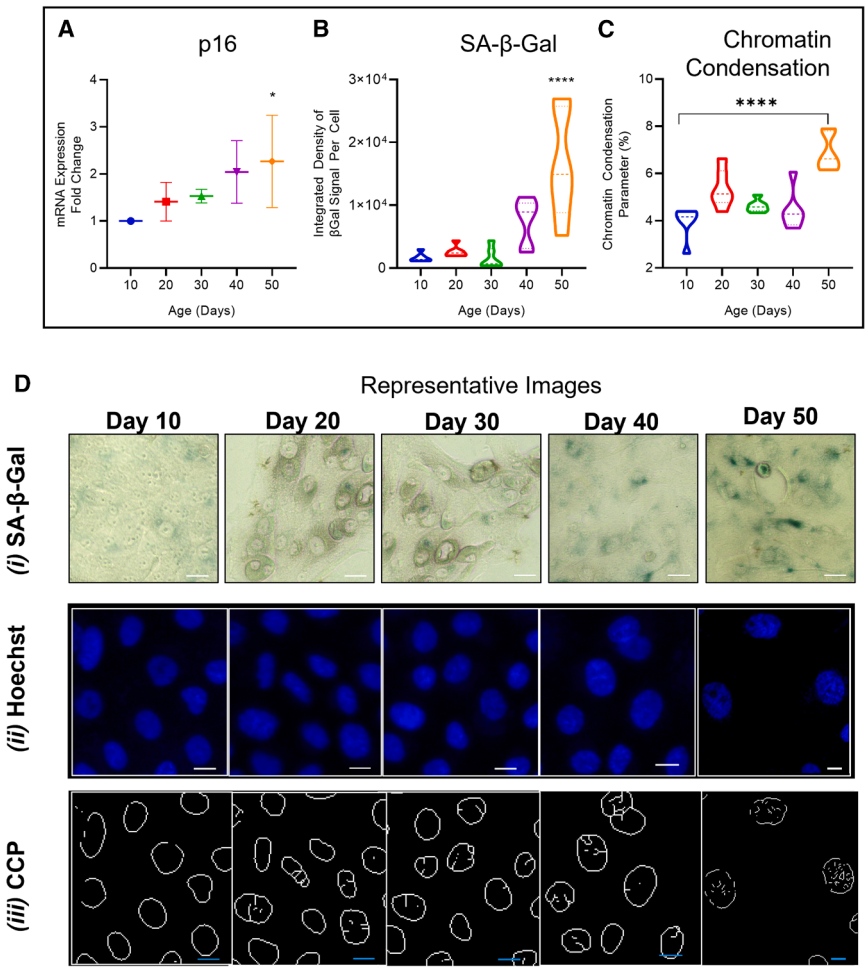

Figure 2. Senescence biomarkers are elevated in 50-day keratinocyte cultures

Human epidermal keratinocytes were thawed and plated into 6-well plates for $p16^{INK4A}$ mRNA expression analysis and into 96-well plates for quantification of SA-β-Gal and chromatin condensation levels.

(A) RT-qPCR analysis revealed a ∼2-fold increase in $p16^{INK4A}$ mRNA levels in 50-day cultures relative to 10-day cultures ($p < 0.05$, $n = 4$ biological replicates).

(B) SA-β-Gal staining was quantified by calculating the integrated density of inverted-stain images in ImageJ, normalized to the number of nuclei per field. Results showed a 9.8-fold increase in 50-day cultures compared to 10-day cultures ($p < 0.0001$, $n = 6$ biological replicates).

(C) Chromatin condensation was assessed using the chromatin condensation parameter (CCP), a metric that quantifies intra-nuclear edge density in Hoechst-stained images. CCP serves as a proxy for detecting senescence-associated heterochromatin foci (SAHFs). 50-day cultures exhibited the highest CCP values, indicating increased chromatin compaction ($0.001 < p < 0.05$, $n = 6$ biological replicates).

(D) Representative images of (i) SA-β-Gal staining, (ii) Hoechst nuclear staining, and (iii) CCP edge-detection overlays, showing progressive chromatin condensation and SA-β-Gal accumulation with time in culture. Scale bars, 10 μm. Violin plots (B,C) display the distribution of biological replicates, with the thick central dashed line representing the mean and the dotted lines indicating the 75th and 25th percentiles. Scatterplots show individual biological replicates with error bars representing the standard deviation.

Statistical significance was assessed using unpaired two-tailed t-tests and Dunn's multiple comparisons test, as indicated; scale bars, 10 μm.

Senescent keratinocytes are less responsive and less resilient to induced changes of V_{mem}

We next investigated senescence-dependent changes in responsiveness of keratinocytes to bioelectric signals, which is of relevance both to the design of external interventions via electroceutical drugs[46,78–80], and to the understanding of responsiveness of cells to endogenous bioelectric signals *in vivo*.[34] To trigger a V_{mem} change, we used the hyperpolarizing drug pinacidil—a KATP channel activator.[81] We acquired images of keratinocytes stained with BeRST pre- and post-treatment to calculate the percentage change in fluorescence Lifetime (Figure 3A). Keratinocytes progressively exhibited greater absolute percentage change in Lifetime, peaking at −42% response on day 30 ($p < 0.0001$, $n = 3$ biological replicates). However, by day 40 keratinocytes appear to have the most diminished response level (Δ-8.9%), albeit statistically not significantly different than day 10 (Figure 3A). In 50-day cultures, keratinocytes responded by depolarizing (Figure 3A) when exposed to pinacidil (Δ+16.9%). These data show that keratinocytes become increasingly more responsive to pinacidil treatment up to day 30; however, once they approach and achieve senescence (Figure 3A), they become not only less responsive but also depolarize when given a hyperpolarizing stimulus.

To determine the presence of senescence-dependent changes in keratinocyte's resilience to V_{mem} perturbations, we calculated the level of timeseries' variance post treatment with pinacidil (Figure 3B). In system dynamics, resilience is the ability of a complex system to adapt to a new equilibrium post perturbation.[1] A system that is resilient will quickly and effectively adjust to a new setpoint, exhibiting little variance[1]; conversely, a frail system will struggle with adjusting to a new setpoint, exhibiting greater variance in its response. The variance of each culture time point was calculated by using the standard deviation of each timeseries. Figure 3B shows 50-day cells having the highest level of variance ($\sigma = 33$, representing standard deviation) compared to earlier time points ($\sigma < 10$) exposed to pinacidil ($p < 0.05$ days 10-day $n = 3$ biological replicates, vs. 50-day $n = 8$ biological replicates). Furthermore, 50-day cultures immediately depolarized when given pinacidil followed by hyperpolarization, then showed a gradual progression toward depolarization (Figure 3C). These data reveal that senescent cells have the lowest degree of V_{mem} resilience,

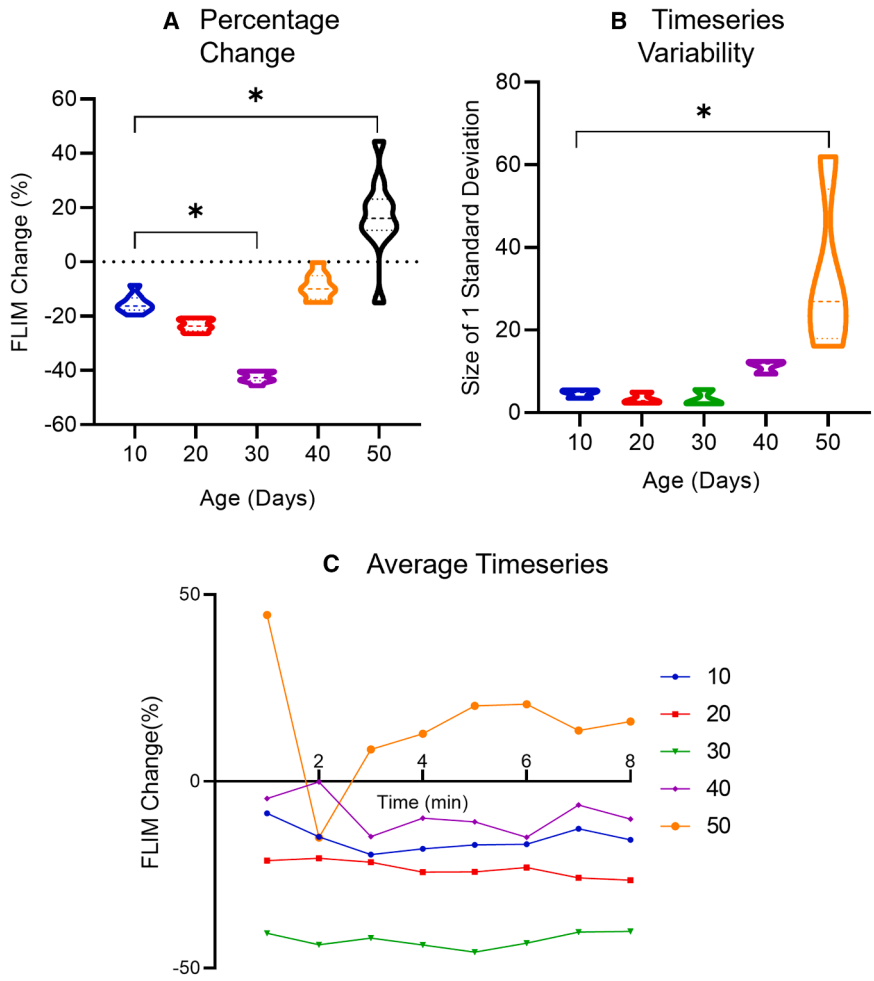

Figure 3. Senescent human epidermal keratinocytes exhibit reduced responsiveness and resilience

Human epidermal keratinocytes were cultured in flat-bottom 96-well plates, stained with 600 nM BeRST, and incubated at 37°C with 5% CO_2 for 30 min. After two PBS washes, cells were imaged using the Leica SP8 confocal microscope. Baseline pre-treatment fluorescence Lifetime images were acquired, followed by immediate treatment with 10 μM pinacidil in fresh media. Percentage change in BeRST Fluorescence Lifetime was calculated relative to the pre-treatment baseline.

(A) Keratinocytes showed peak responsiveness at 30 days in culture (−42%, $p < 0.05$, $n = 3$ biological replicates), followed by a significant decline in response at 40 and 50 days (Δ −8.9% and +16.9%, respectively; $p < 0.0001$, $n = 8$ biological replicates), indicating diminished ability to hyperpolarize in response to pinacidil.

(B) The standard deviation of fluorescence Lifetime timeseries, used as a measure of post-perturbation variance, revealed significantly higher variability in 50-day cultures (σ = 33) compared to earlier time points (σ < 10), indicating reduced resilience (n = 3–8 biological replicates).

(C) Averaged timeseries traces show that keratinocytes from 10 to 40-day cultures hyperpolarized upon pinacidil treatment and maintained a relatively stable bioelectric oscillation. In contrast, 50-day cultures displayed an initial depolarization, a transient hyperpolarization, and a return to depolarized state—indicating impaired ability to maintain stable V_{mem} dynamics. Violin plots (A,B) show the distribution of biological replicates; the thick central dashed line represents the mean, and the dotted lines indicate the 75th and 25th percentiles. Statistical comparisons were performed using Holm-Šídák's multiple comparisons test.

and they fail to achieve a steady hyperpolarized state despite an initial attempt.

Senescent keratinocytes lose ability to form distinct bioelectric domains

We next sought to determine whether cells in culture exhibit large-scale spatial regionalization with respect to V_{mem} (as observed in bioelectric patterns *in vivo*[61,82,83]) and whether this changes with senescence. To this end, we used the voltage-insensitive VoltageFluor 2.0 (VF2.0) and voltage-sensitive VoltageFluor 2.1 (VF2.1), which are analogs of BeRST. These dyes contain a sulfofluorescein fluorophore instead of rhodamine, requiring excitation with 488-nm light. VF2.0 lacks the aniline donor group necessary for photoinduced electron transfer (PeT), rendering it voltage insensitive and suitable as a control for evaluating voltage-independent dye behavior. At higher concentrations, VF2.0 exhibited apparent spatial patterning in fluorescence Lifetime, resembling voltage domains (Figure S1). However, this effect was attributed to concentration-dependent quenching rather than true bioelectric structure. When the concentration was reduced to 50 nM, this domain-like structure was no longer present, and the Lifetime signal appeared randomly distributed (Figure S1). Based on this control, we used 50 nM as the working concentration for VF2.1 in keratinocytes to ensure that spatial autocorrelation analysis would reflect true voltage-sensitive patterns, not dye artifacts.

Surprisingly, we found that even *in vitro*—absent any exogeneous morphogenetic cues as would be present *in vivo*—the cells self-organized into domains (Figure 4). This was particularly apparent in 10-day cultures, as evidenced by the relatively high positive Global Moran's I of 0.5 (Figure 4A). This metric measures the degree of spatial autocorrelation—Moran's I values close to +1 indicate a strong positive spatial correlation, values close to zero indicate random spatial patterning, while negative values imply dissimilar values are adjacent.[84] Furthermore, to investigate whether senescence affects keratinocytes' bioelectric spatial organization, we computed Moran's Global and Local I at each time point. This metric allowed us to quantify the spatial "sharpness" of bioelectric patterns—the crispness with which adjacent regions maintain differences in V_{mem}. Compared to 10-day cultures (n=10 biological replicates), a significant reduction in Moran's I from 0.5 down to 0.13 in 40-day cells ($p < 0.0001$, $n = 7$ biological replicates) and 0.26 in 50-day cells ($p < 0.0001$, $n = 10$ biological replicates) was observed. A reduction in linear regression was also observed when plotting the

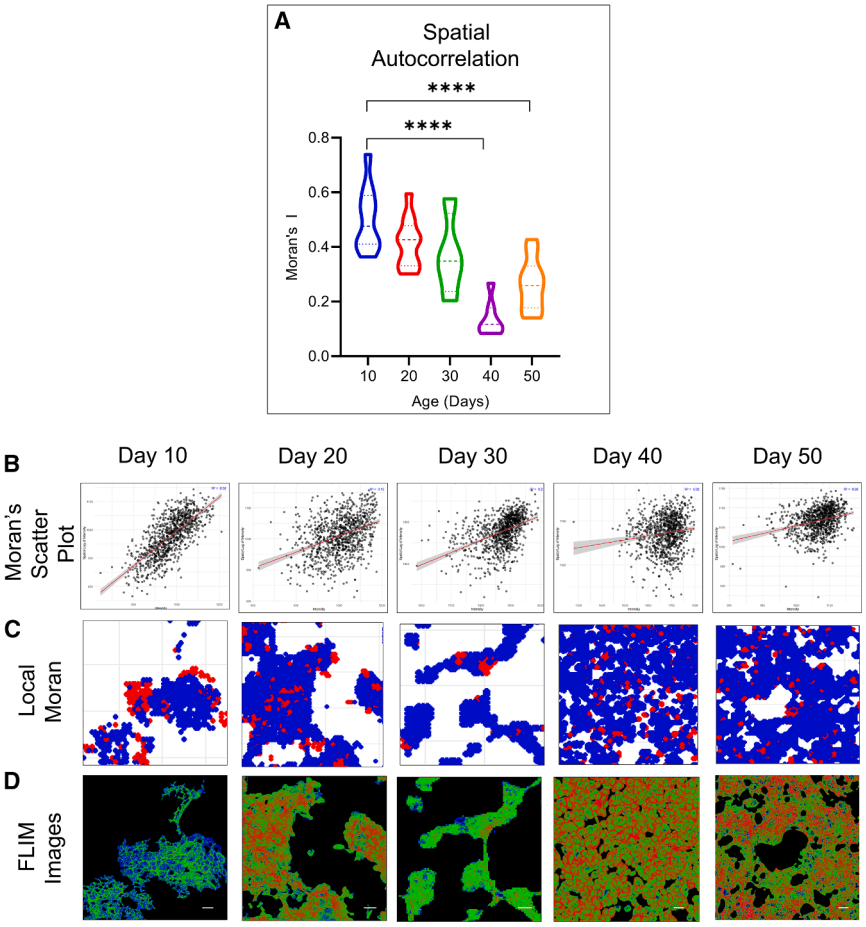

Figure 4. Spatial organization and clustering of membrane potential is reduced with time in culture

Human epidermal keratinocytes were stained with the V_{mem}-sensitive dye VoltageFluor 2.1 (VF2.1, 50 nM) for 30 min at 37°C and 5% CO_2, then washed with PBS and incubated in fresh keratinocyte medium. Fluorescence Lifetime imaging microscopy (FLIM) was performed using a Leica SP8 confocal microscope. Lifetime maps were generated by biexponential curve fitting in the Leica software, thresholded to remove background, and exported as .tif files. A 15 × 15 pixel sliding ROI was used to extract X, Y, and Lifetime values for regions with 100% foreground pixels. To determine the optimal number of nearest neighbors (k) for Moran's I analysis, an elbow test was performed, identifying k = 3 as the inflection point. Data were subsampled to 1000 ROIs and averaged across 10 iterations to control for variation in cell number.

(A) Violin plots show a significant decrease in global Moran's I in 40-day (p = 0.0011, n = 7 biological replicates) and 50-day cultures (p = 0.0005, n = 10 biological replicates) compared to 10-day cultures (n = 10 biological replicates), indicating reduced spatial autocorrelation.

(B) Spatial lag scatterplots of Lifetime vs. spatially lagged Lifetime values illustrate reduced spatial correlation with time in culture. Regression lines flatten from 10-day (R^2 = 0.58) to 40- and 50-day cultures (R^2 = 0.02 and 0.08, respectively), indicating more random spatial patterning.

(C) Local Moran's I maps visualize distinct V_{mem} clusters (red) against non-significant background regions (blue). Cluster size and distribution decline progressively with time in culture, consistent with erosion of spatial patterning.

(D) Representative FLIM images of BeRST-stained keratinocytes corresponding to each time point. Violin plot (A) shows the distribution of biological replicates; the thick central dashed line represents the mean, and the dotted lines indicate the 75th and 25th percentiles. Statistical comparisons were performed using Dunn's multiple comparisons test; scale bars, 10 μm.

Lifetime values against spatially lagged Lifetime (Figure 4B)—the distribution of points became progressively more random with increasing time in culture. Moreover, computing and mapping Local Moran's I revealed a reduction in the size and distribution of distinct clusters with increasing culture duration (Figures 4C and 4D). Taken together these data show a loss of bioelectric spatial organization and reduced spatial heterogeneity (loss of ability to maintain coherent, distinct voltage regions) with increasing time in culture.

Bioelectric modulation of keratinocytes alters senescence-associated phenotypes

To determine whether bioelectricity functions solely as a passive readout or as an active regulator of senescence, we functionally modulated the resting membrane potential of keratinocytes and assessed the resulting changes in senescence biomarkers. We selected 30-day-old cultures for these experiments because, as shown in Figure 3A, these cells exhibited the highest responsiveness to induced V_{mem} changes—making them an ideal window to probe the causal influence of bioelectric modulation before full entry into the senescent state. Cells were treated for six days with either control medium, 10 μM pinacidil (a K_ATP channel opener that hyperpolarizes cells), or 25 mM potassium gluconate (a depolarizing agent). Following treatment, all groups were cultured in control medium for an additional two days prior to imaging. As shown in Figure 5A, pinacidil-treated cultures exhibited a significantly higher number of nuclei ($p < 0.0001$, $n = 18$ biological replicates), whereas potassium gluconate-treated cultures showed reduced cell counts ($p < 0.05$, $n = 24$) relative to control (n = 17). SA-β-Gal staining was markedly increased in the depolarized group ($p < 0.001$, n = 6) compared to control (n = 12), indicating enhanced senescence (Figure 5B). Although pinacidil-treated cells showed reduced SA-β-Gal levels, the difference did not reach statistical significance, likely due to variability in the control group (Figure 5B). Interestingly, potassium-treated cells appeared more solitary and heavily stained (Figure 5G-iii), suggesting a potential disruption in gap junction-mediated intercellular communication. Chromatin condensation analysis (Figure 5C) revealed that pinacidil treatment significantly decreased condensation ($p < 0.05$, $n = 16$), while potassium gluconate significantly increased it ($p < 0.0001$, $n = 16$). The elevated condensation observed in depolarized cells,

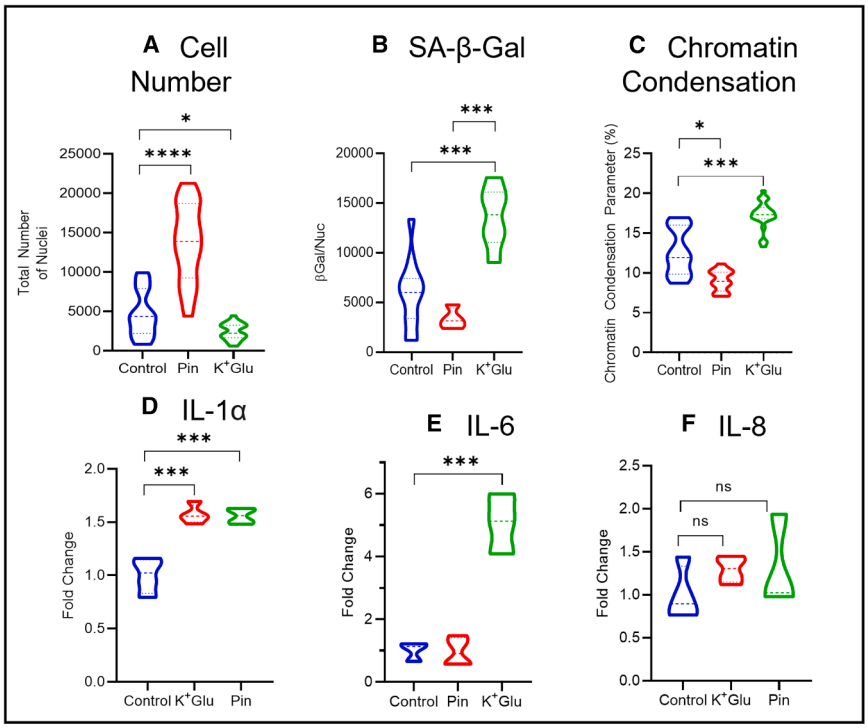

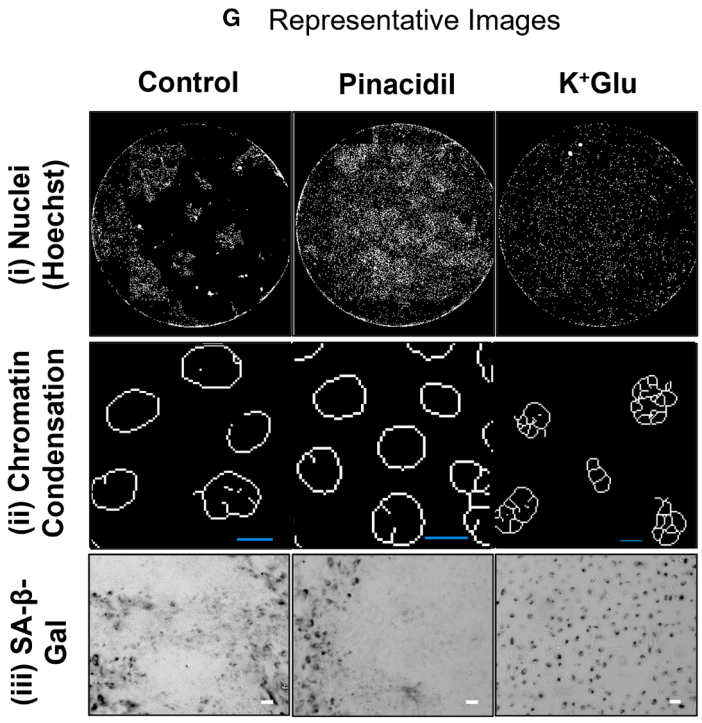

Figure 5. Hyperpolarization reduces, while depolarization increases, senescence-associated phenotypes in keratinocytes

Human epidermal keratinocytes (30 days in culture) were incubated for 6 days in either control medium, medium supplemented with 10 μM pinacidil (hyperpolarizing), or 25 mM potassium gluconate (depolarizing). Media were replaced every 2 days. After 6 days, all groups were switched to control medium for 2 additional days. On day 8, cells were stained with BeRST and Hoechst 33342 and imaged using a Leica SP8 confocal microscope and ImageXpress Confocal HT.ai.

(A) Total number of Hoechst-stained nuclei was significantly higher in pinacidil-treated cultures ($p < 0.0001$, $n = 18$ biological replicates), and significantly lower in potassium gluconate-treated cultures ($p < 0.05$, $n = 24$) relative to control ($n = 17$).

(B) SA-β-Gal per-nucleus signal significantly increased in potassium gluconate-treated cells ($p < 0.001$, $n = 6$) compared to control ($n = 12$). Pinacidil-treated cells showed a reduction compared to the potassium gluconate group ($p < 0.001$), though not statistically different from control.

(C) Chromatin condensation, measured using the chromatin condensation parameter (CCP), significantly increased with depolarization ($p < 0.0001$, $n = 16$) and decreased with hyperpolarization ($p < 0.05$, $n = 16$), compared to control ($n = 18$).

(D–F) Cytokine expression was measured by RT-qPCR. Total RNA was extracted (Qiagen RNeasy Mini Kit), reverse transcribed from 200 ng RNA (iScript cDNA Synthesis Kit), and amplified using SYBR Green Master Mix. Absolute mRNA levels were quantified using a lambda DNA standard curve. Each group included $n = 4$ biological replicates, with technical triplicates. (D) IL-1α was significantly increased in both pinacidil- and potassium gluconate-treated groups ($p < 0.001$). (E) IL-6 increased ~5-fold in depolarized cells only ($p < 0.001$). (F) IL-8 levels were unchanged across groups.

(G) Representative images: (i) Hoechst-stained nuclei, (ii) segmented nuclei used for chromatin condensation analysis, and (iii) SA-β-Gal staining. Scale bar: 10 μm. Violin plots (A-F) show biological replicate distributions; the thick central dashed lines indicate the mean, and the dotted lines represent the 25th and 75th percentiles. Panel A: Holm-Sidak's multiple comparisons test; B: Tukey's multiple comparisons test; (C): Kruskal–Wallis test; (D)–(F): Dunnett's multiple comparisons test; scale bars, 10 μm.

quantified using our edge-detection-based CCP, is consistent with the formation of senescence-associated heterochromatin foci (SAHFs)—a hallmark feature of terminally arrested cells. We next assessed expression of SASP-related cytokines (Figures 5D-5F). IL-1α mRNA levels were elevated in both hyperpolarized and depolarized groups ($p < 0.001$, $n = 4$), suggesting that this inflammatory component may be sensitive to bioelectric shifts despite the direction. However, IL-6 expression was significantly increased only in depolarized cells ($p < 0.001$, $n = 3$), and no significant differences were observed for IL-8. Taken

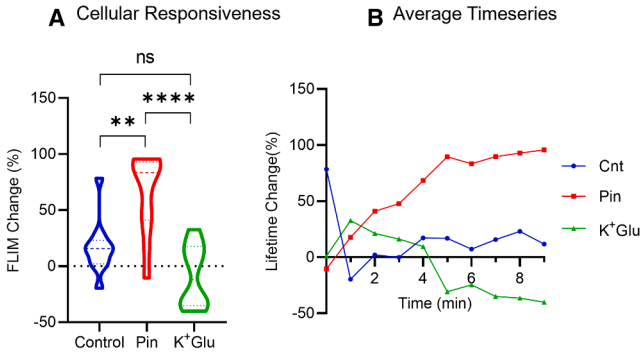

Figure 6. Hyperpolarizing keratinocytes maintains cellular responsiveness

Keratinocytes at 30-day of culture were grown for an additional 6 days in either control media, media containing pinacidil, or potassium gluconate (+25 mM). They were then given fresh control media and grown for another two days, then stained with 600 nM BeRST and 1 μM Hoechst 33432 prior to imaging. (A) The percentage change in BeRST Lifetime was significantly higher in pinacidil treated cells compared to control ($p < 0.01$, control $n = 4$ biological replicates, pinacidil $n = 3$ biological replicates). Treatment with potassium gluconate appeared to decrease the level of responsiveness; however, this was not significantly different than control cells.

(B) Average timeseries of each group reveals control cells appeared to oscillate near 0%, whereas potassium gluconate treated cells progressively became hyperpolarized. Notably, pinacidil treated cells progressively depolarized over time. Violin plot (A) displays biological replicate distributions; the thick central dashed line represents the mean, and the dotted lines indicate the 25th and 75th percentiles. Statistical comparisons were performed using Tukey's multiple comparisons test.

together, these results suggest that bioelectric modulation can directly influence senescence phenotypes: hyperpolarization generally attenuates, while depolarization exacerbates, canonical markers of senescence.

To determine if hyperpolarization of keratinocytes also helped abate diminished cellular responsiveness associated with senescence, we acquired timeseries images of BeRST stained keratinocytes pre- and post-treatment with pinacidil. Our results revealed that keratinocytes pre-treated with pinacidil for 6 days exhibited the greatest degree of responsiveness ($p < 0.01$, control $n = 4$ biological replicates, pinacidil $n = 3$ biological replicates) when exposed to fresh media containing 10 μM of pinacidil (Figure 6A). Conversely, cells pre-treated with elevated potassium levels (+25 mM potassium gluconate) exhibited the lowest levels of responsiveness ($n = 3$ biological replicates), albeit this diminished responsiveness was not statistically significant relative to the control group; however, it is suggestive. Notably, Figure 6B reveals that although pre-treated pinacidil cultures had the highest levels of responsiveness, they in fact progressively depolarized with time. In contrast, pre-treated potassium cells appeared to initially depolarize but then progressively hyperpolarized when exposed to pinacidil. Control cells exhibited an initial recovery from depolarization, followed by oscillation near +10%. Taken together, these data reveal that while hyperpolarization abates diminished cellular responsiveness associated with senescence, the cellular response is altered so that cells depolarize when given hyperpolarizing stimulus.

We next investigate the impact of V_{mem} modulation on bioelectric spatial clustering and organization. Figure 7A reveals no significant difference between control cells and cells pre-treated with pinacidil for 6 days. However, it appears that pre-treatment with elevated potassium ions significantly reduced Moran's I from 0.64 down to 0.26 ($p < 0.01$, control $n = 4$ biological replicates, potassium gluconate $n = 4$ biological replicates). This is also evident in the Lifetime vs. spatial lag Lifetime scatterplots which show pre-treated potassium keratinocytes with a reduced R^2 value of 0.31 vs. 0.67 in the control group, and by the more random distribution of points (Figure 7B). Performing local Moran analysis also revealed that the size and distribution of distinct clusters was significantly reduced (Figures 7C and 7D). These data demonstrate that hyperpolarization via pinacidil did not significantly improve V_{mem} clustering, while depolarization significantly diminished keratinocytes' ability to self-organize in distinct V_{mem} domains.

DISCUSSION

Here, we characterized bioelectric patterns associated with keratinocyte senescence. We determined the relative V_{mem} of keratinocyte stained with the voltage responsive dye, BeRST, while also quantifying senescence biomarkers p16^{INK4A} levels,[71] senescence associated β-galactosidase activity,[72] and senescence associated chromatin condensation. Our results revealed that keratinocytes significantly depolarize after 50 days in culture (Figure 1). This time point coincides with a significant increase in p16^{INK4A} levels, β-galactosidase activity, and chromatin condensation (Figure 2). To further support the presence of senescence rather than a quiescent state, we examined expression of canonical SASP cytokines IL-1α, IL-6, and IL-8.[85,86] Notably, only IL-6 was significantly upregulated in 50-day cultures (Figure S2), while IL-1α and IL-8 remained unchanged. This pattern is consistent with partial SASP activation, a feature observed in context-dependent senescence models,[77] and further supports the interpretation that the bioelectric and structural changes observed are senescence-associated rather than indicative of quiescence. These findings establish membrane depolarization as a robust marker of keratinocyte senescence and are in line with prior studies showing that depolarization can be both a marker and a functional driver of the senescent state.[58,59,87]

We also found that the inter-culture heterogeneity of cells' V_{mem} values (Figure 1B), p16^{INK4A} levels, and SA-β-Gal activity (Figures 2A and 2B) were significantly greater in 40 and 50-day old senescent keratinocyte cultures. Notably, the distribution of both culture time points is bimodal; however, at day 40, the distribution is more equal between depolarized and hyperpolarized values. By day 50, the distribution shifts more toward depolarized values, indicating a greater fraction of the cultures becoming senescent. Paradoxically, we observed a significant reduction in intra-culture V_{mem} heterogeneity at 40 and 50 days relative to earlier time points. This inter-culture variability likely reflects differences in microenvironmental factors—such as nutrient availability, cell density, and paracrine signaling, which influence the timing and extent of senescence induction across dishes.[88] Notably, despite variability between cultures, cells within a given dish consistently converge toward a similar

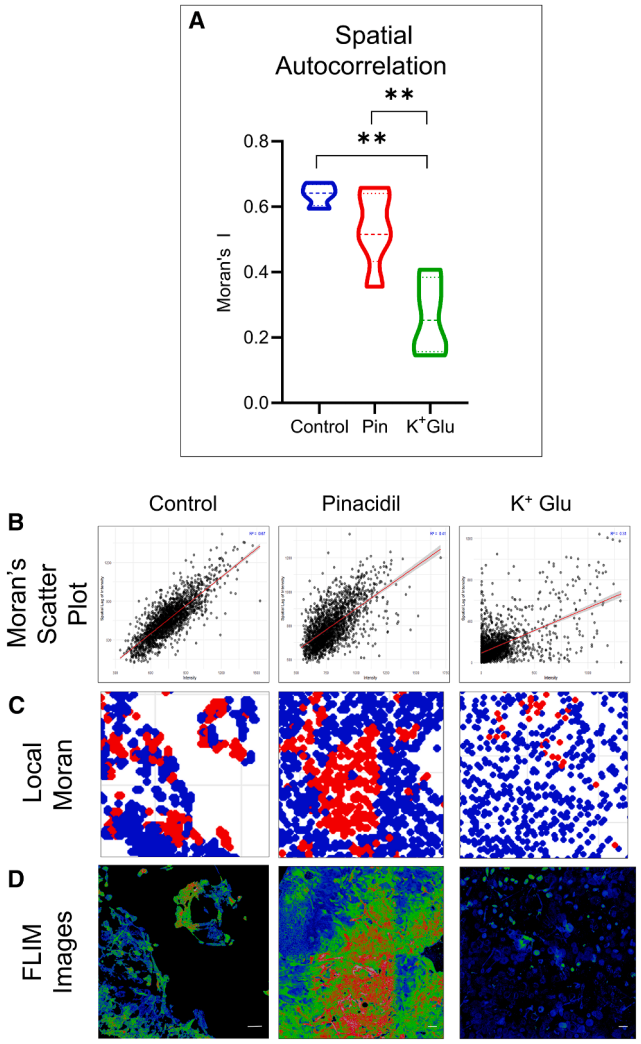

Figure 7. Depolarization of keratinocytes leads to loss of spatial organization and clustering

Keratinocytes at 30-day of culture were grown for an additional 6 days in either control media, media containing pinacidil or potassium gluconate (+25 mM). They were then given fresh control media and grown for another two days; then immediately prior to imaging, cells were stained with 50 nM VF2.1 and 1 μM Hoechst 33342 for 30-min in a humidified incubator at 37°C and 5% CO_2, washed twice with PBS and then given fresh keratinocyte media. Fluorescence Lifetime Imaging was performed with the Leica SP8 Confocal microscope. The collected FLIM images were fitted with biexponential decay curve in the Leica suit, thresholded to remove background, and exported as ".Tif" files for further analysis. A 15 × 15 pixels ROI was used to scan the image and generate an excel file containing "X", "Y", and "Lifetime" for ROIs above 100% "ON" pixels. To determine the appropriate "k" value, i.e., number of clusters, for the Moran's I calculation, we initially ran an elbow test to trial k values from 1 to 10 and determined the elbow of the curve to be at k = 3. To control for differences in cell number, we subsampled our data (1,000 cells) with 10 iterations which was then averaged.

(A) Pre-treatment with pinacidil did not result in a significant change; however, potassium gluconate treatment significantly reduced Moran's I from 0.63 to 0.26 ($p < 0.01$, control $n = 4$ biological replicates, potassium gluconate $n = 4$ biological replicates).

(B) Scatterplot of Lifetime vs. spatial lag Lifetime also revealed a more random distribution of points, consistent with reduced spatial autocorrelation.

(C) Local Moran computation shows reduction in size and distribution of distinct clusters in potassium gluconate pre-treated cells.

(D) Representative images of VF2.1 stained cells showing corresponding clusters. Violin plot (A) displays biological replicate distributions; the thick central dashed lines represent the mean and the dotted lines indicate the 25th and 75th percentiles. Statistical comparisons were performed using Tukey's multiple comparisons test; scale bars, 10 μm.

V_{mem} distribution before fully transitioning into a depolarized state (Figure 1C), suggesting that local microenvironments drive bioelectric homogenization prior to the onset of senescence-associated depolarization.[37,89] *In vivo*, this may mirror how senescence unfolds asynchronously across the epidermis, where keratinocytes reside in spatially distinct niches that differ in mechanical tension, oxygen availability, cytokine exposure, and morphogen gradients.[90,91] These spatial cues could cause localized convergence of membrane potential among neighboring cells, resulting in patchy distributions of senescent, depolarized cells within a broader, heterogeneous tissue landscape.

It is known that senescent cells exhibit substantial variability in gene expression due to differences in upstream stressors, epigenetic states, and pathway activation.[92] Several pathways can initiate senescence through membrane depolarization. Upstream of this shift in membrane potential, signaling pathways such as mTORC1 have been shown to upregulate sodium channels like SCN1A, increasing sodium influx and driving depolarization.[58,93] Similarly, oncogenic or inflammatory activation of the nuclear factor kappa B (NF-κB) pathway increases SCN9A expression, further promoting sodium-driven depolarization.[59] Additionally, PPP3R1—a regulatory subunit of calcineurin—promotes membrane depolarization, likely through modulation of ion channel activity, which in turn facilitates calcium influx and activates calcineurin signaling to drive senescence.[57] Once depolarized, cells exhibit increased calcium influx through voltage-gated calcium channels, triggering downstream effectors, such as NFAT, ATF3, and p53.[57,58] In parallel, SCN9A-mediated depolarization engages the Rb pathway and represses mitotic gene expression.[59] This convergence on a common depolarized state suggests that V_{mem} functions as a low-dimensional emergent phenotype—meaning that it is a stable, scalar readout arising from the collective activity of a limited set of ion channels and pumps, even as gene expression remains high-dimensional and variable. In other words, while senescent cells diverge in transcriptional signatures, they converge on a common electrical state, likely reflecting the presence of a bioelectric attractor state that reinforces and stabilizes the senescent phenotype. This supports the idea that membrane potential acts as an upstream integrator of cellular state, buffering against transcriptional noise and coordinating the transition into senescence.[87]

Homeostatic processes, such as the ones that enable cells to cooperate toward reaching and maintaining a specific large-scale target morphology, can fail in one of several ways. For example, they can lose setpoint information, and/or they can become unable to implement the error minimization steps even if the setpoint information is available to them. Thus, over time, one way in which the on-going maintenance of the body can be disrupted is through progressive degradation of

bioelectrically encoded information. Our data on V_{mem} changes during senescence is consistent with this. Another possible failure point of the morphological homeostasis cycle *in vivo* could be diminished responsiveness of individual cells to signals that drive collective behavior.[2] It is known that with increasing age, cells have a reduced response to growth factors,[94] hormones,[95] immune signals,[96] and even nutrients (*e.g.*, aged muscle cells show reduced sensitivity to amino acids such as leucine[97]). Here we investigated whether the ability to implement instructive bioelectrical signals likewise reduces over time, by determining cells' responsiveness to a V_{mem}-altering drug. We characterized, at different culture durations, the V_{mem} of cells pre- and post-treatment with pinacidil—KATP agonist[81] (Figure 3). Results show that keratinocytes become increasingly more responsive to hyperpolarization until day 30; however, upon approaching and achieving senescence on 40–50 days of culture, a significant reduction in responsiveness is observed (Figure 3). In fact, it appears that 50-day old senescent cultures undergo depolarization rather than hyperpolarization when exposed to pinacidil. Immediately after exposure to pinacidil, 50-day old senescent cultures became depolarized and then they ostensibly attempt a correction with hyperpolarization; however, they seem unable to maintain a hyperpolarized state. These data suggest that even if senescing cells produce and receive the signals needed to maintain tissue-level bioelectrical order, they may be incapable of responding appropriately. If this phenomenon holds *in vivo*, then it would mean that senescent cells contribute to disrupting tissue homeostasis not only by their diminished responsivity to bioelectric/morphogenetic cues, but also by executing the wrong response. The accumulation of these senescent cells in tissue would increasingly lead to a progressive loss of morphostatic information stored in bioelectric gradients. These data also reveal that bioelectric interventions aiming to prevent senescence should target keratinocytes when they are most responsive to hyperpolarization (30-days of culture) rather than attempting to rescue unresponsive senescent cells.

The resilience of a system is measured by how quickly and effectively it can converge or diverge from its equilibrium after perturbation.[1] Stochastic resilience theory incorporates the randomness of biological systems and therefore investigates the distribution of the system around equilibrium.[1] Here, we sought to investigate how the resilience of keratinocyte bioelectrics changes with culture duration. One resilience metric is the variance of a timeseries after perturbation – greater variance indicates lower resilience.[1] To this end, we performed a timeseries acquisition pre- and post-treatment with Pinacidil. Our results revealed that 50-day old senescing cells exhibit the greatest degree of variance in V_{mem} (Figures 3B and 3C). These data reveal that senescent cells have significantly reduced resilience preventing them from quickly and effectively reaching a new homeostatic setpoint. The presence of such frail cells would expectedly introduce noise to the system, diminishing the ability to collectively coordinate their V_{mem}, and possibly reducing the system's ability to navigate through morphospace, because bioelectric patterns and their integration with downstream transcriptional and other mechanisms require significant temporal coordination to maintain longevity and optimal function.

The presence of frail senescent cells in culture or in tissue may consequently result in the degradation of instructive spatial bioelectric patterns. To investigate whether the spatial organization of bioelectric patterns changed over time in culture, we computed Moran's Global and Local I, as well as linear regression analysis of Lifetime vs. spatial-lag Lifetime for each time point. Moran's I, which ranges from −1 to +1, is a measure of spatial autocorrelation and consequently the degree of spatial clustering and organization present.[84,98] A high Moran's I indicates strong spatial clustering of similar V_{mem} values; values closer to zero indicate randomness, and values close to negative one indicate negative clustering, *i.e.*, cells with dissimilar V_{mem} values neighbor each other. Computing Moran's I for keratinocytes of different times in culture revealed a time-dependent decrease in Moran's I, reaching the lowest degree in 40- and 50-day cultures (Figure 4A). Plotting the Lifetime values of cells against the spatial lag-Lifetime values, which reveals whether there is strong linear regression, showed higher levels of linear regression in earlier time points, and a progressive reduction with time, reaching the lowest at 40- and 50-day cultures (Figure 4B). Moreover, computation and mapping of Local Moran's I revealed a progressive reduction in the size and distribution of distinct V_{mem} clusters over time in culture (Figure 4B). This loss of spatial structure coincided with reduced intra-culture variability (Figure 1C), suggesting that as cells converge toward a uniform depolarized state, their ability to form distinct bioelectric domains diminishes. Taken together, these data indicate that the spatial organization of membrane potential in keratinocyte monolayers erodes with time in culture, supporting the morphostatic information loss theory, in which sharp differences between regions of distinct V_{mem} become blurred—a phenomenon also observed in various developmental defects.[36–38] One notable feature of these data is that bioelectric regionalization exists at all, *in vitro*. While domains of different V_{mem}, demarcating developmental compartments, are well-known in the context of complex morphogenesis *in vivo*,[61,82,99–104] it is surprising to find them in the absence of organizing centers. While the origin and significance of *in vitro* bioelectric patterns are as yet unknown, it is likely that they indicate the innate tendency of patterns to emerge via symmetry-breaking and self-organization in the excitable media of bioelectrically active and sensitive cells.[105–109]

To determine whether bioelectricity plays an instructive role in senescence rather than serving merely as a correlative biomarker, we experimentally modulated the resting membrane potential of keratinocytes and examined the resulting impact on senescence-associated phenotypes. As shown in Figure 5, 30-day cells were cultured for six days in either control medium, hyperpolarizing medium containing pinacidil, or depolarizing medium containing elevated potassium ions. Hyperpolarization significantly increased proliferation and reduced chromatin condensation levels. Although pinacidil-treated cells also showed an approximate 50% reduction in SA-β-Gal staining, this difference was not statistically significant, likely due to variability in the control group. In contrast, depolarized cells exhibited reduced proliferation, elevated SA-β-Gal activity, and increased chromatin condensation. Taken together, these data demonstrate that hyperpolarization attenuates, while

depolarization exacerbates, senescence-associated phenotypes. These findings are consistent with previous reports showing that membrane hyperpolarization can delay the onset of senescence, whereas depolarization promotes senescence marker expression.[58,59]

Interestingly, potassium gluconate-treated keratinocytes also appeared more disconnected from one another, particularly among cells with strong SA-β-Gal staining (Figure 5G-iii). Within the same cultures, cells with low SA-β-Gal activity often remained in clusters, suggesting that highly senescent cells may become bioelectrically isolated. This is reminiscent of cancer cells, which frequently lose gap junctional communication and become refractory to higher-order morphogenetic signals.[110] Indeed, cancer cells are also characteristically more depolarized than their non-transformed counterparts.[111,112] Though seemingly paradoxical, this discrepancy may reflect distinct V_{mem} "windows" that differentially regulate cell fate. It is possible that moderate depolarization promotes proliferation, while further depolarization drives senescence. Supporting this, Mathews et al.[110] demonstrated that pharmacological agents that further depolarize glioblastoma cells can induce senescence and arrest, underscoring a context- and threshold-dependent role of membrane potential in determining cell fate.

In addition to morphological and proliferative changes, modulation of membrane potential also influenced the expression of SASP-related cytokines (Figures 5D-5F). Both hyperpolarization and depolarization significantly increased IL-1α mRNA levels, suggesting that IL-1α may be a general stress-responsive factor[113] sensitive to V_{mem} fluctuations, regardless of direction. However, IL-6 was selectively upregulated in depolarized cells, aligning with its well-established role as a key effector of the senescence-associated secretory phenotype.[77,114] No significant changes were observed in IL-8 expression under either condition. These data suggest that membrane potential not only regulates canonical senescence markers, but also exerts pathway-specific control over inflammatory signaling.

We next characterized pre-treated keratinocytes' responsiveness to ascertain whether modulation of the resting membrane potential also helped abate diminished cellular responsiveness associated with senescence (Figure 6A). Our results revealed that pre-treatment with hyperpolarization resulted in keratinocytes with the highest level of responsivity (Figure 6A). However, these cells underwent depolarization rather than hyperpolarization when given fresh pinacidil (Figure 6B). This could be due to compensatory mechanisms activated during the chronic exposure to pinacidil over the 6 days. These data imply that future bioelectric modulations should possibly employ multiple hyperpolarizing drugs with different mechanisms of action to overcome the compensatory mechanisms of cells. Pre-treatment with depolarization resulted in the lowest responsivity; however, this was not statistically significant. Taking together, these data demonstrate that bioelectric interventions can abate senescent-associated diminished responsivity.

We then characterized the spatial organization of cells pre-treated with depolarization or hyperpolarization (Figure 7). We expected that depolarization would lead to a reduction, while hyperpolarization would lead to an increase in spatial V_{mem} clustering and organization. Our results show that compared to control cells, depolarization treatment did lead to significant reduction in spatial organization and clustering. However, pinacidil treatment did not increase spatial autocorrelation but instead led to a non-statistically significant reduction. These data reveal that depolarization diminishes cells' ability to collectively organize and cluster in distinct V_{mem} domains, revealing a possible role of gap-junction disruption during senescence. Indeed, gap-junction (cx43) mRNA and protein levels are reportedly downregulated in aged human umbilical vein endothelial cells.[115] Our data also reveal that treatment with pinacidil did not enhance spatial autocorrelation as expected. This may be due to the fact that pinacidil prevented the onset of senescence on an individual cell level but did not work to drive collective cell behavior.

These findings carry important implications for therapeutic strategies targeting aging-related conditions. Current senolytic and senomorphic approaches aim to either eliminate or reprogram senescent cells but often face challenges due to cell-type specificity, tissue heterogeneity, and off-target effects.[116,117] Our data suggest that modulating bioelectric states—particularly through controlled hyperpolarization—offers a complementary, potentially upstream intervention point, as has been seen in the context of bioelectric signals inducing whole organs,[118] and triggering complex transcriptional and cell behavioral cascades in the context of birth defects repair[36] and cancer normalization.[119] By targeting membrane potential before cells become unresponsive or fully committed to senescence, it may be possible to delay or prevent the accumulation of dysfunctional cells that compromise tissue homeostasis. In the context of skin aging where keratinocyte senescence contributes to epidermal thinning, impaired barrier function, and reduced regenerative capacity,[120,121] restoring bioelectric balance may help maintain epithelial integrity and responsiveness. The skin also represents a uniquely tractable tissue for bioelectric intervention, given its accessibility to topical agents, wearable devices, and localized electrical stimulation.[79,122] Our *in vitro* model of keratinocyte aging provides a relevant and scalable platform to explore such interventions and screen for bioelectric modulators that could be deployed non-invasively. Moreover, because membrane potential integrates multiple cellular inputs and influences diverse outputs—from proliferation to SASP expression—bioelectric modulation may provide a unified approach to broadly tune aging-related phenotypes across tissues. Future strategies may leverage electroceuticals such as ion channel-targeting drugs[123–125] or bioelectric devices[126–128] to preserve or restore bioelectric gradients, thereby enhancing tissue resilience and extending health span.

The present study characterizes the bioelectrics of senescing keratinocytes, both in terms of the membrane potential (V_{mem}) patterns they generate and of their declining capacity to respond to bioelectric modulation. We observed culture time-dependent shifts toward depolarization, reduced spatial organization, diminished responsiveness, and loss of bioelectric resilience—each pointing to a breakdown in the coordinated electrical signaling that underpins tissue-level homeostasis. These changes are consistent with the core predictions of the "loss of morphostatic information" theory of aging,[2] which posits that the progressive erosion of instructive bioelectric patterns

contributes to age-related dysfunction. More broadly, it points to the involvement of tractable biophysical parameters that may represent attractive endpoints for modulation. Future work will explore how spatial and temporal features of V_{mem} are interpreted by cells, and whether these pathways can be harnessed or restored for therapeutic rejuvenation.

Limitations of the study

While our findings establish membrane depolarization as a robust marker and functional contributor to keratinocyte senescence, several limitations remain. First, our *in vitro* monolayer culture system lacks the full complexity of the *in vivo* epidermal niche, including immune interactions, extracellular matrix context, and mechanical stress gradients. As such, the extent to which bioelectric pattern erosion occurs in aged human skin tissues remains to be validated. Second, partial SASP activation suggests context-dependent transcriptional regulation by V_{mem}, but the specific pathways linking membrane potential to cytokine expression remain unresolved. Third, while pinacidil and potassium gluconate modulate V_{mem} effectively, they may exert off-target effects; thus, future work using additional ion channel modulators or genetic approaches will be necessary to dissect causal mechanisms with greater specificity.

RESOURCE AVAILABILITY

Lead contact

Further information and requests for information should be directed to and will be fulfilled by the lead contact, Dr. Michael Levin (michael.levin@tufts.edu).

Material availability

No new materials or cell lines were generated in this study.

Data and code availability

- The dataset associated with this study is available at the Harvard Dataverse: Sediqi, Hamid; Levin, Michael, 2024, "Replication Data for: Bioelectric Characterization of Senescing Human Keratinocytes", https://doi.org/10.7910/DVN/NEU8UO.
- Custom R and Python scripts for Moran's I and clustering analysis are provided as Data S1 and S2.
- Any additional information required to reanalyze the data reported in this paper are available from the lead contact upon request.

ACKNOWLEDGMENTS

We thank Evan W. Miller for his invaluable assistance with voltage imaging dyes, Patrick McMillian for his feedback on earlier drafts of this work, and Julia Poirier for assistance with the manuscript. M.L. gratefully acknowledges funding via sponsored research agreement with Astonishing Labs Inc.

AUTHOR CONTRIBUTIONS

H.S., conceptualization, methodology, investigation, formal analysis, data curation, visualization, writing – original draft, writing – review and editing; M.L., supervision, funding acquisition, project administration, writing – review and editing.

DECLARATION OF INTERESTS

The authors declare no competing interests.

STAR★METHODS

Detailed methods are provided in the online version of this paper and include the following:

- KEY RESOURCES TABLE
- EXPERIMENTAL MODEL AND STUDY PARTICIPANT DETAILS
- METHOD DETAILS
  - Cell culture
  - Bioelectric imaging of resting voltage potential
  - Spatial autocorrelation imaging and analysis (Moran's I)
  - Chromatin Condensation Parameter (CCP) quantification
  - Senescence-associated β-galactosidase (SA-β-Gal) assay
  - RT-qPCR
- QUANTIFICATION AND STATISTICAL ANALYSIS

SUPPLEMENTAL INFORMATION

Supplemental information can be found online at https://doi.org/10.1016/j.isci.2025.113275.

Received: February 27, 2025
Revised: May 16, 2025
Accepted: July 30, 2025
Published: August 7, 2025

REFERENCES

1. Cohen, A.A., Ferrucci, L., Fülöp, T., Gravel, D., Hao, N., Kriete, A., Levine, M.E., Lipsitz, L.A., Olde Rikkert, M.G.M., Rutenberg, A., et al. (2022). A complex systems approach to aging biology. Nat. Aging *2*, 580–591. https://doi.org/10.1038/s43587-022-00252-6.
2. Pio-Lopez, L., and Levin, M. (2024). Aging as a loss of morphostatic information: A developmental bioelectricity perspective. Ageing Res. Rev. *97*, 102310. https://doi.org/10.1016/j.arr.2024.102310.
3. Freitas, A.A., and de Magalhães, J.P. (2011). A review and appraisal of the DNA damage theory of ageing. Mutat. Res. *728*, 12–22. https://doi.org/10.1016/j.mrrev.2011.05.001.
4. Gladyshev, V.N., Kritchevsky, S.B., Clarke, S.G., Cuervo, A.M., Fiehn, O., de Magalhães, J.P., Mau, T., Maes, M., Moritz, R., Niedernhofer, L.J., et al. (2021). Molecular Damage in Aging. Nat. Aging *1*, 1096–1106. https://doi.org/10.1038/s43587-021-00150-3.
5. Kirkwood, T.B.L., and Melov, S. (2011). On the programmed/non-programmed nature of ageing within the life history. Curr. Biol. *21*, R701–R707. https://doi.org/10.1016/j.cub.2011.07.020.
6. Trubitsyn, A.G. (2020). The Mechanism of Programmed Aging: The Way to Create a Real Remedy for Senescence. Curr. Aging Sci. *13*, 31–41. https://doi.org/10.2174/1874609812666191014111422.
7. Tenchov, R., Sasso, J.M., Wang, X., and Zhou, Q.A. (2024). Antiaging Strategies and Remedies: A Landscape of Research Progress and Promise. ACS Chem. Neurosci. *15*, 408–446. https://doi.org/10.1021/acschemneuro.3c00532.
8. Lu, Y.R., Tian, X., and Sinclair, D.A. (2023). The Information Theory of Aging. Nat. Aging *3*, 1486–1499. https://doi.org/10.1038/s43587-023-00527-6.
9. Rubin, H. (2007). Ordered heterogeneity and its decline in cancer and aging. Adv. Cancer Res. *98*, 117–147. https://doi.org/10.1016/S0065-230X(06)98004-X.
10. Rubin, H. (2006). What keeps cells in tissues behaving normally in the face of myriad mutations? Bioessays *28*, 515–524. https://doi.org/10.1002/bies.20403.
11. Rubin, H. (1994). Cellular epigenetics: control of the size, shape, and spatial distribution of transformed foci by interactions between the transformed and nontransformed cells. Proc. Natl. Acad. Sci. USA *91*, 1039–1043. https://doi.org/10.1073/pnas.91.3.1039.

12. Chow, M., Yao, A., and Rubin, H. (1994). Cellular epigenetics: topochronology of progressive "spontaneous" transformation of cells under growth constraint. Proc. Natl. Acad. Sci. USA *91*, 599–603. https://doi.org/10.1073/pnas.91.2.599.

13. Rubin, H. (1993). Cellular epigenetics: effects of passage history on competence of cells for "spontaneous" transformation. Proc. Natl. Acad. Sci. USA *90*, 10715–10719. https://doi.org/10.1073/pnas.90.22.10715.

14. Fields, C., and Levin, M. (2022). Competency in Navigating Arbitrary Spaces as an Invariant for Analyzing Cognition in Diverse Embodiments. Entropy *24*, 819. https://doi.org/10.3390/e24060819.

15. Pezzulo, G., and Levin, M. (2015). Re-membering the body: applications of computational neuroscience to the top-down control of regeneration of limbs and other complex organs. Integr. Biol. *7*, 1487–1517. https://doi.org/10.1039/c5ib00221d.

16. Levin, M. (2021). Bioelectric signaling: Reprogrammable circuits underlying embryogenesis, regeneration, and cancer. Cell *184*, 1971–1989. https://doi.org/10.1016/j.cell.2021.02.034.

17. Bates, E. (2015). Ion channels in development and cancer. Annu. Rev. Cell Dev. Biol. *31*, 231–247. https://doi.org/10.1146/annurev-cellbio-100814-125338.

18. Harris, M.P. (2021). Bioelectric signaling as a unique regulator of development and regeneration. Development *148*, dev180794. https://doi.org/10.1242/dev.180794.

19. Sundelacruz, S., Levin, M., and Kaplan, D.L. (2009). Role of membrane potential in the regulation of cell proliferation and differentiation. Stem Cell Rev. Rep. *5*, 231–246. https://doi.org/10.1007/s12015-009-9080-2.

20. Blackiston, D.J., McLaughlin, K.A., and Levin, M. (2009). Bioelectric controls of cell proliferation: ion channels, membrane voltage and the cell cycle. Cell Cycle *8*, 3527–3536. https://doi.org/10.4161/cc.8.21.9888.

21. Pai, V.P., Martyniuk, C.J., Echeverri, K., Sundelacruz, S., Kaplan, D.L., and Levin, M. (2016). Genome-wide analysis reveals conserved transcriptional responses downstream of resting potential change in Xenopus embryos, axolotl regeneration, and human mesenchymal cell differentiation. Regeneration *3*, 3–25. https://doi.org/10.1002/reg2.48.

22. Lang, F., Föller, M., Lang, K.S., Lang, P.A., Ritter, M., Gulbins, E., Vereninov, A., and Huber, S.M. (2005). Ion channels in cell proliferation and apoptotic cell death. J. Membr. Biol. *205*, 147–157.

23. Schwab, A., and Stock, C. (2014). Ion channels and transporters in tumour cell migration and invasion. Philos. Trans. R. Soc. Lond. B Biol. Sci. *369*, 20130102. https://doi.org/10.1098/rstb.2013.0102.

24. Chen, L., Hassani Nia, F., and Stauber, T. (2021). Ion Channels and Transporters in Muscle Cell Differentiation. Int. J. Mol. Sci. *22*, 13615. https://doi.org/10.3390/ijms222413615.

25. Li, B., Jie, W., Huang, L., Wei, P., Li, S., Luo, Z., Friedman, A.K., Meredith, A.L., Han, M.H., Zhu, X.H., and Gao, T.M. (2014). Nuclear BK channels regulate gene expression via the control of nuclear calcium signaling. Nat. Neurosci. *17*, 1055–1063. https://doi.org/10.1038/nn.3744.

26. Galva, C., Artigas, P., and Gatto, C. (2012). Nuclear Na+/K+-ATPase plays an active role in nucleoplasmic Ca2+ homeostasis. J. Cell Sci. *125*, 6137–6147. https://doi.org/10.1242/jcs.114959.

27. Chen, Y., Sánchez, A., Rubio, M.E., Kohl, T., Pardo, L.A., and Stühmer, W. (2011). Functional K(v)10.1 channels localize to the inner nuclear membrane. PLoS One *6*, e19257. https://doi.org/10.1371/journal.pone.0019257.

28. Mazzanti, M., Bustamante, J.O., and Oberleithner, H. (2001). Electrical dimension of the nuclear envelope. Physiol. Rev. *81*, 1–19. https://doi.org/10.1152/physrev.2001.81.1.1.

29. Mathews, J., and Levin, M. (2017). Gap junctional signaling in pattern regulation: Physiological network connectivity instructs growth and form. Dev. Neurobiol. *77*, 643–673. https://doi.org/10.1002/dneu.22405.

30. Wang, E.T., and Zhao, M. (2010). Regulation of tissue repair and regeneration by electric fields. Chin. J. Traumatol. *13*, 55–61. https://doi.org/10.3760/cma.j.issn.1008-1275.2010.01.011.

31. Zhao, M. (2009). Electrical fields in wound healing-An overriding signal that directs cell migration. Semin. Cell Dev. Biol. *20*, 674–682. https://doi.org/10.1016/j.semcdb.2008.12.009.

32. George, L.F., and Bates, E.A. (2022). Mechanisms Underlying Influence of Bioelectricity in Development. Front. Cell Dev. Biol. *10*, 772230. https://doi.org/10.3389/fcell.2022.772230.

33. Levin, M. (2014). Molecular bioelectricity: how endogenous voltage potentials control cell behavior and instruct pattern regulation *in vivo*. Mol. Biol. Cell *25*, 3835–3850. https://doi.org/10.1091/mbc.E13-12-0708.

34. Levin, M., and Martyniuk, C.J. (2018). The bioelectric code: An ancient computational medium for dynamic control of growth and form. Biosystems *164*, 76–93. https://doi.org/10.1016/j.biosystems.2017.08.009.

35. Pai, V.P., and Levin, M. (2022). HCN2 channel-induced rescue of brain, eye, heart and gut teratogenesis caused by nicotine, ethanol and aberrant notch signalling. Wound Repair Regen. *30*, 681–706. https://doi.org/10.1111/wrr.13032.

36. Pai, V.P., Pietak, A., Willocq, V., Ye, B., Shi, N.Q., and Levin, M. (2018). HCN2 Rescues brain defects by enforcing endogenous voltage pre-patterns. Nat. Commun. *9*, 998. https://doi.org/10.1038/s41467-018-03334-5.

37. Pai, V.P., Lemire, J.M., Paré, J.F., Lin, G., Chen, Y., and Levin, M. (2015). Endogenous gradients of resting potential instructively pattern embryonic neural tissue via Notch signaling and regulation of proliferation. J. Neurosci. *35*, 4366–4385. https://doi.org/10.1523/JNEUROSCI.1877-14.2015.

38. Pai, V.P., Lemire, J.M., Chen, Y., Lin, G., and Levin, M. (2015). Local and long-range endogenous resting potential gradients antagonistically regulate apoptosis and proliferation in the embryonic CNS. Int. J. Dev. Biol. *59*, 327–340. https://doi.org/10.1387/ijdb.150197ml.

39. Rubin, H., Chow, M., and Yao, A. (1996). Cellular aging, destabilization, and cancer. Proc. Natl. Acad. Sci. USA *93*, 1825–1830. https://doi.org/10.1073/pnas.93.5.1825.

40. Lobikin, M., Chernet, B., Lobo, D., and Levin, M. (2012). Resting potential, oncogene-induced tumorigenesis, and metastasis: the bioelectric basis of cancer *in vivo*. Phys. Biol. *9*, 065002. https://doi.org/10.1088/1478-3975/9/6/065002.

41. Chernet, B., and Levin, M. (2013). Endogenous Voltage Potentials and the Microenvironment: Bioelectric Signals that Reveal, Induce and Normalize Cancer. J Clin Exp Oncol *Suppl*. J. Clin. Exp. Oncol. *1*, S1-002. https://doi.org/10.4172/2324-9110.S1-002.

42. Chernet, B.T., and Levin, M. (2013). Transmembrane voltage potential is an essential cellular parameter for the detection and control of tumor development in a Xenopus model. Dis. Model. Mech. *6*, 595–607. https://doi.org/10.1242/dmm.010835.

43. Prevarskaya, N., Skryma, R., and Shuba, Y. (2018). Ion Channels in Cancer: Are Cancer Hallmarks Oncochannelopathies? Physiol. Rev. *98*, 559–621. https://doi.org/10.1152/physrev.00044.2016.

44. Foust, A.J., Quicke, P.E.H., Sun, Y., Bakal, C., and Djamgoz, M.B.A. (2023). Voltage-Sensitive Optical Probes for Measuring Cell Membrane Potentials: An Update and Applications to "Nonexcitable" Cells. Bioelectricity *5*, 250–265. https://doi.org/10.1089/bioe.2022.0034.

45. Payne, S.L., Levin, M., and Oudin, M.J. (2019). Bioelectric Control of Metastasis in Solid Tumors. Bioelectricity *1*, 114–130. https://doi.org/10.1089/bioe.2019.0013.

46. Levin, M., Selberg, J., and Rolandi, M. (2019). Endogenous Bioelectrics in Development, Cancer, and Regeneration: Drugs and Bioelectronic Devices as Electroceuticals for Regenerative Medicine. iScience *22*, 519–533. https://doi.org/10.1016/j.isci.2019.11.023.

47. McLaughlin, K.A., and Levin, M. (2018). Bioelectric signaling in regeneration: Mechanisms of ionic controls of growth and form. Dev. Biol. *433*, 177–189. https://doi.org/10.1016/j.ydbio.2017.08.032.

48. Pchelintseva, E., and Djamgoz, M.B.A. (2018). Mesenchymal stem cell differentiation: Control by calcium-activated potassium channels. J. Cell. Physiol. *233*, 3755–3768. https://doi.org/10.1002/jcp.26120.

49. Sundelacruz, S., Levin, M., and Kaplan, D.L. (2013). Depolarization alters phenotype, maintains plasticity of predifferentiated mesenchymal stem cells. Tissue Eng. Part A *19*, 1889–1908. https://doi.org/10.1089/ten.tea.2012.0425.rev.

50. Sundelacruz, S., Moody, A.T., Levin, M., and Kaplan, D.L. (2019). Membrane Potential Depolarization Alters Calcium Flux and Phosphate Signaling During Osteogenic Differentiation of Human Mesenchymal Stem Cells. Bioelectricity *1*, 56–66. https://doi.org/10.1089/bioe.2018.0005.

51. Sundelacruz, S., Levin, M., and Kaplan, D.L. (2015). Comparison of the depolarization response of human mesenchymal stem cells from different donors. Sci. Rep. *5*, 18279. https://doi.org/10.1038/srep18279.

52. Bhuyan, A.K., Varshney, A., and Mathew, M.K. (2001). Resting membrane potential as a marker of apoptosis: studies on Xenopus oocytes microinjected with cytochrome c. Cell Death Differ. *8*, 63–69. https://doi.org/10.1038/sj.cdd.4400773.

53. Nelson, M.T., and Quayle, J.M. (1995). Physiological roles and properties of potassium channels in arterial smooth muscle. Am. J. Physiol. *268*, C799–C822. https://doi.org/10.1152/ajpcell.1995.268.4.C799.

54. Rühl, P., Langner, J.M., Reidel, J., Schönherr, R., Hoshi, T., and Heinemann, S.H. (2021). Monitoring of compound resting membrane potentials of cell cultures with ratiometric genetically encoded voltage indicators. Commun. Biol. *4*, 1164. https://doi.org/10.1038/s42003-021-02675-0.

55. McMillen, P., and Levin, M. (2024). Optical Estimation of Bioelectric Patterns in Living Embryos. Methods Mol. Biol. *2745*, 91–102. https://doi.org/10.1007/978-1-0716-3577-3_6.

56. Kirk, M.J., Raliski, B.K., and Miller, E.W. (2020). Monitoring neuronal activity with voltage-sensitive fluorophores. Methods Enzymol. *640*, 185–204. https://doi.org/10.1016/bs.mie.2020.04.028.

57. Li, M., Gong, W., Chen, J., Zhang, Y., Ma, Y., and Tu, X. (2023). PPP3R1 Promotes MSCs Senescence by Inducing Plasma Membrane Depolarization and Increasing Ca(2+) Influx. Int. J. Mol. Sci. *24*, 4421. https://doi.org/10.3390/ijms24054421.

58. Chen, A., Jin, J., Cheng, S., Liu, Z., Yang, C., Chen, Q., Liang, W., Li, K., Kang, D., Ouyang, Z., et al. (2022). mTORC1 induces plasma membrane depolarization and promotes preosteoblast senescence by regulating the sodium channel Scn1a. Bone Res. *10*, 25. https://doi.org/10.1038/s41413-022-00204-1.

59. Warnier, M., Flaman, J.M., Chouabe, C., Wiel, C., Gras, B., Griveau, A., Blanc, E., Foy, J.P., Mathot, P., Saintigny, P., et al. (2018). The SCN9A channel and plasma membrane depolarization promote cellular senescence through Rb pathway. Aging Cell *17*, e12736. https://doi.org/10.1111/acel.12736.

60. Whited, J.L., and Levin, M. (2019). Bioelectrical controls of morphogenesis: from ancient mechanisms of cell coordination to biomedical opportunities. Curr. Opin. Genet. Dev. *57*, 61–69. https://doi.org/10.1016/j.gde.2019.06.014.

61. Vandenberg, L.N., Morrie, R.D., and Adams, D.S. (2011). V-ATPase-dependent ectodermal voltage and pH regionalization are required for craniofacial morphogenesis. Dev. Dyn. *240*, 1889–1904. https://doi.org/10.1002/dvdy.22685.

62. Park, S.C., Lee, Y.S., Cho, K.A., Kim, S.Y., Lee, Y.I., Lee, S.R., and Lim, I. K. (2023). What matters in aging is signaling for responsiveness. Pharmacol. Ther. *252*, 108560. https://doi.org/10.1016/j.pharmthera.2023.108560.

63. Laboratories, S.R. (2025). Human Epidermal Keratinocytes-Neonatal (HEKn). https://sciencellonline.com/en/human-epidermal-keratinocytes-neonatal/.

64. Eckert, R.L., Efimova, T., Dashti, S.R., Balasubramanian, S., Deucher, A., Crish, J.F., Sturniolo, M., and Bone, F. (2002). Keratinocyte survival, differentiation, and death: many roads lead to mitogen-activated protein kinase. J. Investig. Dermatol. Symp. Proc. *7*, 36–40. https://doi.org/10.1046/j.1523-1747.2002.19634.x.

65. Gruber, F., Kremslehner, C., Eckhart, L., and Tschachler, E. (2020). Cell aging and cellular senescence in skin aging - Recent advances in fibroblast and keratinocyte biology. Exp. Gerontol. *130*, 110780. https://doi.org/10.1016/j.exger.2019.110780.

66. Huang, Y.L., Walker, A.S., and Miller, E.W. (2015). A Photostable Silicon Rhodamine Platform for Optical Voltage Sensing. J. Am. Chem. Soc. *137*, 10767–10776. https://doi.org/10.1021/jacs.5b06644.

67. Walker, A.S., Raliski, B.K., Karbasi, K., Zhang, P., Sanders, K., and Miller, E.W. (2021). Optical Spike Detection and Connectivity Analysis With a Far-Red Voltage-Sensitive Fluorophore Reveals Changes to Network Connectivity in Development and Disease. Front. Neurosci. *15*, 643859. https://doi.org/10.3389/fnins.2021.643859.

68. McMillen, P., and Levin, M. (2024). Optical Estimation of Bioelectric Patterns in Living Embryos (Springer US), pp. 91–102. https://doi.org/10.1007/978-1-0716-3577-3_6.

69. Lazzari-Dean, J.R., Gest, A.M., and Miller, E.W. (2019). Optical estimation of absolute membrane potential using fluorescence lifetime imaging. eLife *8*, e44522. https://doi.org/10.7554/eLife.44522.

70. Liu, P., and Miller, E.W. (2020). Electrophysiology, Unplugged: Imaging Membrane Potential with Fluorescent Indicators. Acc. Chem. Res. *53*, 11–19. https://doi.org/10.1021/acs.accounts.9b00514.

71. LaPak, K.M., and Burd, C.E. (2014). The molecular balancing act of p16(INK4a) in cancer and aging. Mol. Cancer Res. *12*, 167–183. https://doi.org/10.1158/1541-7786.MCR-13-0350.

72. Hartmann, C., Herling, L., Hartmann, A., Köckritz, V., Fuellen, G., Walter, M., and Hermann, A. (2023). Systematic estimation of biological age of *in vitro* cell culture systems by an age-associated marker panel. Front. Aging *4*, 1129107. https://doi.org/10.3389/fragi.2023.1129107.

73. Shaban, H.A., and Gasser, S.M. (2025). Dynamic 3D genome reorganization during senescence: defining cell states through chromatin. Cell Death Differ. *32*, 9–15. https://doi.org/10.1038/s41418-023-01197-y.

74. Sosnik, J., Vieira, W.A., Webster, K.A., Siegfried, K.R., and McCusker, C. D. (2017). A new and improved algorithm for the quantification of chromatin condensation from microscopic data shows decreased chromatin condensation in regenerating axolotl limb cells. PLoS One *12*, e0185292. https://doi.org/10.1371/journal.pone.0185292.

75. Irianto, J., Lee, D.A., and Knight, M.M. (2014). Quantification of chromatin condensation level by image processing. Med. Eng. Phys. *36*, 412–417. https://doi.org/10.1016/j.medengphy.2013.09.006.

76. Aird, K.M., and Zhang, R. (2013). Detection of senescence-associated heterochromatin foci (SAHF). Methods Mol. Biol. *965*, 185–196. https://doi.org/10.1007/978-1-62703-239-1_12.

77. Basisty, N., Kale, A., Jeon, O.H., Kuehnemann, C., Payne, T., Rao, C., Holtz, A., Shah, S., Sharma, V., Ferrucci, L., et al. (2020). A proteomic atlas of senescence-associated secretomes for aging biomarker development. PLoS Biol. *18*, e3000599. https://doi.org/10.1371/journal.pbio.3000599.

78. Djamgoz, M.B.A. (2024). Electrical excitability of cancer cells-CELEX model updated. Cancer Metastasis Rev. *43*, 1579–1591. https://doi.org/10.1007/s10555-024-10195-6.

79. Balasubramanian, S., Weston, D.A., Levin, M., and Davidian, D.C.C. (2024). Electroceuticals: emerging applications beyond the nervous system and excitable tissues. Trends Pharmacol. Sci. *45*, 391–394. https://doi.org/10.1016/j.tips.2024.03.001.

80. Churchill, C.D.M., Winter, P., Tuszynski, J.A., and Levin, M. (2019). EDEn-Electroceutical Design Environment: Ion Channel Tissue Expression Database with Small Molecule Modulators. iScience *11*, 42–56. https://doi.org/10.1016/j.isci.2018.12.003.

81. Cao, C., Healey, S., Amaral, A., Lee-Couture, A., Wan, S., Kouttab, N., Chu, W., and Wan, Y. (2007). ATP-sensitive potassium channel: a novel target for protection against UV-induced human skin cell damage. J. Cell. Physiol. *212*, 252–263. https://doi.org/10.1002/jcp.21026.

82. Weiß, I., and Bohrmann, J. (2019). Electrochemical patterns during Drosophila oogenesis: ion-transport mechanisms generate stage-specific gradients of pH and membrane potential in the follicle-cell epithelium. BMC Dev. Biol. *19*, 12. https://doi.org/10.1186/s12861-019-0192-x.

83. Durant, F., Morokuma, J., Fields, C., Williams, K., Adams, D.S., and Levin, M. (2017). Long-Term, Stochastic Editing of Regenerative Anatomy via Targeting Endogenous Bioelectric Gradients. Biophys. J. *112*, 2231–2243. https://doi.org/10.1016/j.bpj.2017.04.011.

84. Schmal, C., Myung, J., Herzel, H., and Bordyugov, G. (2017). Moran's I quantifies spatio-temporal pattern formation in neural imaging data. Bioinformatics *33*, 3072–3079. https://doi.org/10.1093/bioinformatics/btx351.

85. Kuilman, T., Michaloglou, C., Vredeveld, L.C.W., Douma, S., van Doorn, R., Desmet, C.J., Aarden, L.A., Mooi, W.J., and Peeper, D.S. (2008). Oncogene-induced senescence relayed by an interleukin-dependent inflammatory network. Cell *133*, 1019–1031. https://doi.org/10.1016/j.cell.2008.03.039.

86. Coppé, J.P., Desprez, P.Y., Krtolica, A., and Campisi, J. (2010). The senescence-associated secretory phenotype: the dark side of tumor suppression. Annu. Rev. Pathol. *5*, 99–118. https://doi.org/10.1146/annurev-pathol-121808-102144.

87. Venkatachalam, K. (2022). Regulation of Aging and Longevity by Ion Channels and Transporters. Cells *11*, 1180. https://doi.org/10.3390/cells11071180.

88. Acosta, J.C., Banito, A., Wuestefeld, T., Georgilis, A., Janich, P., Morton, J.P., Athineos, D., Kang, T.W., Lasitschka, F., Andrulis, M., et al. (2013). A complex secretory program orchestrated by the inflammasome controls paracrine senescence. Nat. Cell Biol. *15*, 978–990. https://doi.org/10.1038/ncb2784.

89. Levin, M. (2014). Endogenous bioelectrical networks store non-genetic patterning information during development and regeneration. J. Physiol. *592*, 2295–2305. https://doi.org/10.1113/jphysiol.2014.271940.

90. Ge, Y., and Fuchs, E. (2018). Stretching the limits: from homeostasis to stem cell plasticity in wound healing and cancer. Nat. Rev. Genet. *19*, 311–325. https://doi.org/10.1038/nrg.2018.9.

91. Yu, G.T., Ganier, C., Allison, D.B., Tchkonia, T., Khosla, S., Kirkland, J.L., Lynch, M.D., and Wyles, S.P. (2025). Mapping epidermal and dermal cellular senescence in human skin aging. Aging Cell *24*, e14358. https://doi.org/10.1111/acel.14358.

92. Wiley, C.D., Flynn, J.M., Morrissey, C., Lebofsky, R., Shuga, J., Dong, X., Unger, M.A., Vijg, J., Melov, S., and Campisi, J. (2017). Analysis of individual cells identifies cell-to-cell variability following induction of cellular senescence. Aging Cell *16*, 1043–1050. https://doi.org/10.1111/acel.12632.

93. Carroll, B., Nelson, G., Rabanal-Ruiz, Y., Kucheryavenko, O., Dunhill-Turner, N.A., Chesterman, C.C., Zahari, Q., Zhang, T., Conduit, S.E., Mitchell, C.A., et al. (2017). Persistent mTORC1 signaling in cell senescence results from defects in amino acid and growth factor sensing. J. Cell Biol. *216*, 1949–1957. https://doi.org/10.1083/jcb.201610113.

94. Matsuda, T., Okamura, K., Sato, Y., Morimoto, A., Ono, M., Kohno, K., and Kuwano, M. (1992). Decreased response to epidermal growth factor during cellular senescence in cultured human microvascular endothelial cells. J. Cell. Physiol. *150*, 510–516. https://doi.org/10.1002/jcp.1041500311.

95. Palmer, A.K., Xu, M., Zhu, Y., Pirtskhalava, T., Weivoda, M.M., Hachfeld, C.M., Prata, L.G., van Dijk, T.H., Verkade, E., Casaclang-Verzosa, G., et al. (2019). Targeting senescent cells alleviates obesity-induced metabolic dysfunction. Aging Cell *18*, e12950. https://doi.org/10.1111/acel.12950.

96. Marrella, V., Facoetti, A., and Cassani, B. (2022). Cellular Senescence in Immunity against Infections. Int. J. Mol. Sci. *23*, 11845. https://doi.org/10.3390/ijms231911845.

97. Dardevet, D., Rieu, I., Fafournoux, P., Sornet, C., Combaret, L., Bruhat, A., Mordier, S., Mosoni, L., and Grizard, J. (2003). Leucine: a key amino acid in ageing-associated sarcopenia? Nutr. Res. Rev. *16*, 61–70. https://doi.org/10.1079/NRR200252.

98. Qiu, Z., Li, S., Luo, M., Zhu, S., Wang, Z., and Jiang, Y. (2022). Detection of differentially expressed genes in spatial transcriptomics data by spatial analysis of spatial transcriptomics: A novel method based on spatial statistics. Front. Neurosci. *16*, 1086168. https://doi.org/10.3389/fnins.2022.1086168.

99. Schotthöfer, S.K., and Bohrmann, J. (2020). Analysing bioelectrical phenomena in the Drosophila ovary with genetic tools: tissue-specific expression of sensors for membrane potential and intracellular pH, and RNAi-knockdown of mechanisms involved in ion exchange. BMC Dev. Biol. *20*, 15. https://doi.org/10.1186/s12861-020-00220-6.

100. Weiß, I., and Bohrmann, J. (2019). Electrochemical gradients are involved in regulating cytoskeletal patterns during epithelial morphogenesis in the Drosophila ovary. BMC Dev. Biol. *19*, 22. https://doi.org/10.1186/s12861-019-0203-y.

101. Telfer, W.H., Woodruff, R.I., and Huebner, E. (1981). Electrical Polarity and Cellular-Differentiation in Meroistic Ovaries. Am. Zool. *21*, 675–686. https://doi.org/10.1093/icb/21.3.675.

102. Woodruff, R.I., and Telfer, W.H. (1980). Electrophoresis of proteins in intercellular bridges. Nature *286*, 84–86. https://doi.org/10.1038/286084a0.

103. Jaffe, L.F., and Woodruff, R.I. (1979). Large electrical currents traverse developing Ceropia follicles. Proc. Natl. Acad. Sci. USA *76*, 1328–1332. https://doi.org/10.1073/pnas.76.3.1328.

104. Woodruff, R.I., and Telfer, W.H. (1974). Electrical properties of ovarian cells linked by intercellular bridges. Ann. N. Y. Acad. Sci. *238*, 408–419. https://doi.org/10.1111/j.1749-6632.1974.tb26807.x.

105. Cervera, J., Meseguer, S., and Mafé, S. (2018). Intercellular Connectivity and Multicellular Bioelectric Oscillations in Nonexcitable Cells: A Biophysical Model. ACS Omega *3*, 13567–13575. https://doi.org/10.1021/acsomega.8b01514.

106. Cervera, J., Pai, V.P., Levin, M., and Mafé, S. (2019). From non-excitable single-cell to multicellular bioelectrical states supported by ion channels and gap junction proteins: Electrical potentials as distributed controllers. Prog. Biophys. Mol. Biol. *149*, 39–53. https://doi.org/10.1016/j.pbiomolbio.2019.06.004.

107. Cervera, J., Manzanares, J.A., Mafé, S., and Levin, M. (2019). Synchronization of Bioelectric Oscillations in Networks of Nonexcitable Cells: From Single-Cell to Multicellular States. J. Phys. Chem. B *123*, 3924–3934. https://doi.org/10.1021/acs.jpcb.9b01717.

108. Pietak, A., and Levin, M. (2017). Bioelectric gene and reaction networks: computational modelling of genetic, biochemical and bioelectrical dynamics in pattern regulation. J. R. Soc. Interface *14*, 20170425. https://doi.org/10.1098/rsif.2017.0425.

109. Pietak, A., and Levin, M. (2016). Exploring Instructive Physiological Signaling with the Bioelectric Tissue Simulation Engine. Front. Bioeng. Biotechnol. *4*, 55. https://doi.org/10.3389/fbioe.2016.00055.

110. Mathews, J., Kuchling, F., Baez-Nieto, D., Diberardinis, M., Pan, J.Q., and Levin, M. (2022). Ion Channel Drugs Suppress Cancer Phenotype in NG108-15 and U87 Cells: Toward Novel Electroceuticals for Glioblastoma. Cancers *14*, 1499. https://doi.org/10.3390/cancers14061499.

111. Stevenson, D., Binggeli, R., Weinstein, R.C., Keck, J.G., Lai, M.C., and Tong, M.J. (1989). Relationship between Cell-Membrane Potential and Natural-Killer Cell Cytolysis in Human Hepatocellular-Carcinoma Cells. Cancer Res. *49*, 4842–4845.

112. Srivastava, P., Kane, A., Harrison, C., and Levin, M. (2021). A Meta-Analysis of Bioelectric Data in Cancer, Embryogenesis, and Regeneration. Bioelectricity *3*, 42–67. https://doi.org/10.1089/bioe.2019.0034.

113. Rider, P., Carmi, Y., Guttman, O., Braiman, A., Cohen, I., Voronov, E., White, M.R., Dinarello, C.A., and Apte, R.N. (2011). IL-1alpha and IL-1beta recruit different myeloid cells and promote different stages of sterile inflammation. J. Immunol. *187*, 4835–4843. https://doi.org/10.4049/jimmunol.1102048.

114. Paldor, M., Levkovitch-Siany, O., Eidelshtein, D., Adar, R., Enk, C.D., Marmary, Y., Elgavish, S., Nevo, Y., Benyamini, H., Plaschkes, I., et al. (2022). Single-cell transcriptomics reveals a senescence-associated IL-6/CCR6 axis driving radiodermatitis. EMBO Mol. Med. *14*, e15653. https://doi.org/10.15252/emmm.202115653.

115. Xie, H.Q., and Hu, V.W. (1994). Modulation of gap junctions in senescent endothelial cells. Exp. Cell Res. *214*, 172–176. https://doi.org/10.1006/excr.1994.1246.

116. Di Micco, R., Krizhanovsky, V., Baker, D., and d'Adda di Fagagna, F. (2021). Cellular senescence in ageing: from mechanisms to therapeutic opportunities. Nat. Rev. Mol. Cell Biol. *22*, 75–95. https://doi.org/10.1038/s41580-020-00314-w.

117. Kirkland, J.L., and Tchkonia, T. (2020). Senolytic drugs: from discovery to translation. J. Intern. Med. *288*, 518–536. https://doi.org/10.1111/joim.13141.

118. Pai, V.P., Aw, S., Shomrat, T., Lemire, J.M., and Levin, M. (2012). Transmembrane voltage potential controls embryonic eye patterning in Xenopus laevis. Development *139*, 313–323. https://doi.org/10.1242/dev.073759.

119. Chernet, B.T., and Levin, M. (2014). Transmembrane voltage potential of somatic cells controls oncogene-mediated tumorigenesis at long-range. Oncotarget *5*, 3287–3306. https://doi.org/10.18632/oncotarget.1935.

120. Rittié, L., and Fisher, G.J. (2015). Natural and sun-induced aging of human skin. Cold Spring Harb. Perspect. Med. *5*, a015370. https://doi.org/10.1101/cshperspect.a015370.

121. Victorelli, S., Lagnado, A., Halim, J., Moore, W., Talbot, D., Barrett, K., Chapman, J., Birch, J., Ogrodnik, M., Meves, A., et al. (2019). Senescent human melanocytes drive skin ageing via paracrine telomere dysfunction. EMBO J. *38*, e101982. https://doi.org/10.15252/embj.2019101982.

122. Evans, J.P., and Sen, C.K. (2023). Electrochemical Devices in Cutaneous Wound Healing. Bioengineering *10*, 711. https://doi.org/10.3390/bioengineering10060711.

123. Kofman, K., and Levin, M. (2024). Bioelectric pharmacology of cancer: A systematic review of ion channel drugs affecting the cancer phenotype. Prog. Biophys. Mol. Biol. *191*, 25–39. https://doi.org/10.1016/j.pbiomolbio.2024.07.005.

124. Tuszynski, J., Tilli, T.M., and Levin, M. (2017). Ion Channel and Neurotransmitter Modulators as Electroceutical Approaches to the Control of Cancer. Curr. Pharm. Des. *23*, 4827–4841. https://doi.org/10.2174/1381612823666170530105837.

125. Kale, V.P., Amin, S.G., and Pandey, M.K. (2015). Targeting ion channels for cancer therapy by repurposing the approved drugs. Biochim. Biophys. Acta *1848*, 2747–2755. https://doi.org/10.1016/j.bbamem.2015.03.034.

126. Marquez, G., Dechiraju, H., Baniya, P., Li, H., Tebyani, M., Pansodtee, P., Jafari, M., Barbee, A., Orozco, J., Teodorescu, M., et al. (2024). Delivering biochemicals with precision using bioelectronic devices enhanced with feedback control. PLoS One *19*, e0298286. https://doi.org/10.1371/journal.pone.0298286.

127. Dechiraju, H., Li, Y., Comerci, C., Luo, L., Figuerres, S., Asefi, N., Trevino, A., Barbee, A., Tebyani, M., Baniya, P., et al. (2025). Bioelectronic Delivery of Potassium Ions Controls Membrane Voltage and Growth Dynamics in Bacteria Biofilms. Biomed. Mater. Devices *3*, 646–654. https://doi.org/10.1007/s44174-024-00209-w.

128. Asefifeyzabadi, N., Nguyen, T., Li, H., Zhu, K., Yang, H.Y., Baniya, P., Medina Lopez, A., Gallegos, A., Hsieh, H.C., Dechiraju, H., et al. (2024). A pro-reparative bioelectronic device for controlled delivery of ions and biomolecules. Wound Repair Regen. *32*, 709–719. https://doi.org/10.1111/wrr.13191.

129. Rutledge, R.G. (2011). A Java program for LRE-based real-time qPCR that enables large-scale absolute quantification. PLoS One *6*, e17636. https://doi.org/10.1371/journal.pone.0017636.

130. Krzystyniak, A., Gluchowska, A., Mosieniak, G., and Sikora, E. (2023). Fiji-Based Tool for Rapid and Unbiased Analysis of SA-beta-Gal Activity in Cultured Cells. Biomolecules *13*, 362. https://doi.org/10.3390/biom13020362.

STAR★METHODS

KEY RESOURCES TABLE

REAGENT or RESOURCE	SOURCE	IDENTIFIER
Chemicals, peptides, and recombinant proteins		
SYBR™ Green Master Mix	Thermo Fisher Scientific	Cat# A25777
iScript™ cDNA Synthesis Kit	Bio-Rad	Cat# 1725035
RNeasy Mini Kit	Qiagen	Cat# 74104
SA-β-Gal Staining Kit	Cell Signaling Technologies	Cat# 9860
VF2.0.Cl	Gift from Dr. Evan Miller (UC Berkeley)	N/A
VF2.1.Cl	Gift from Dr. Evan Miller (UC Berkeley)	N/A
BeRST dye	Gift from Dr. Evan Miller (UC Berkeley)	N/A
Poly-L-lysine (PLL)	ScienceCell	Cat# 0403
Keratinocyte Medium	ScienceCell	Cat# 2101
Hoechst 33342	Thermo Fisher Scientific	Cat# H3570
Deposited data		
Raw Data	This Paper	https://doi.org/10.7910/DVN/NEU8UO
Experimental models: Cell lines		
Human Epidermal Keratinocytes–neonatal (HEK-n)	ScienceCell	Cat# 2100
Oligonucleotides		
p16INK4A: Fwd – CTCGTGCTGATGCTACTGAGGA; Rev – GGTCGGCGCAGTTGGGCTCC	IDT; designed via NCBI Primer-BLAST	N/A
IL1-α: Fwd – TGTATGTGACTGCCCAAGATGAAG; Rev – AGAGGAGGTTGGTCTCACTACC	IDT; designed via NCBI Primer-BLAST	N/A
IL6: Fwd – AGACAGCCACTCACCTCTTCAG; Rev – TTCTGCCAGTGCCTCTTTGCTG	IDT; designed via NCBI Primer-BLAST	N/A
IL8: Fwd – GAGAGTGATTGAGAGTGGACCAC; Rev – CACAACCCTCTGCACCCAGTTT	IDT; designed via NCBI Primer-BLAST	N/A
Lambda DNA (standard): Fwd – CTGCTGGCCGGAA CTAATGAATTTATTGGT; Rev – ATGCCACGATGCCT CATCACTGTTG	Rutledge[129]	N/A
Software and algorithms		
Custom Python Scripts for Moran's I	This paper	In supplemental
RStudio	Posit (formerly RStudio, PBC)	https://posit.co/
GraphPad Prism	GraphPad Software	https://www.graphpad.com
ImageJ	NIH	https://imagej.nih.gov/ij/
Other		
EVOS M7000 Imaging System	Thermo Fisher Scientific	N/A
ImageXpress® Confocal HT.ai	Molecular Devices	N/A
Leica SP8 Confocal Microscope	Leica Microsystems	N/A
NCBI BLAST tools	NIH	

EXPERIMENTAL MODEL AND STUDY PARTICIPANT DETAILS

Human Epidermal Keratinocytes–neonatal (HEK-n) were purchased from ScienceCell Research Laboratories (Cat# 2100). These primary cells are derived from neonatal foreskin tissue isolated from a single donor. The sex of the donor was not specified by the manufacturer.

METHOD DETAILS

Cell culture

HEK-n cells were cultured in T75 flasks pre-coated with poly-L-lysine (PLL; ScienceCell Cat# 0403) and maintained using keratinocyte medium (ScienceCell Cat# 2101) in a humidified incubator at 37 °C and 5% CO_2. The medium was replaced every 48 hours. Cells were initially seeded at ~20% confluency (~2.2×10^4 cells/cm^2) and passaged at ~80% confluency (~9.0×10^4 cells/cm^2) using a 1:5 split ratio. This expansion and passaging cycle was repeated continuously. At each target culture duration (10, 20, 30, 40, and 50 days), a portion of cells was cryopreserved in keratinocyte medium supplemented with 10% DMSO. The approximate passage numbers for each timepoint were passage 2 (day 10), passage 4 (day 20), passage 6 (day 30), passage 7 (day 40), and passage 8 (day 50). According to the manufacturer, all HEK-n cells are tested for: viability, cell morphology, proliferation capacity, cytokeratin expression (CK14) by immunocytochemistry, negative for HIV-1, HBV, HCV, mycoplasma, bacteria, yeast, and fungi. The cells are not immortalized and are intended for research use only. Authentication by short tandem repeat (STR) profiling was not performed by the authors. RRID is not available for this cell line as of June 2025. These cells were used in all experiments described in this study. All cell culture manipulations were performed under sterile conditions in a biosafety cabinet using standard aseptic techniques.

Bioelectric imaging of resting voltage potential

To measure resting membrane potential (V_{mem}), HEK-n cells were thawed from cryopreservation and seeded onto 10-cm^2 culture dishes containing 20 mL of keratinocyte medium. Cells were incubated at 37 °C with 5% CO_2 for 6 hours, after which the medium was replaced to remove residual DMSO. Cells were then cultured for 7 days, then seeded into 96-well plates precoated with poly-L-lysine at least 48 hours before imaging. Cells were incubated with 600 nM BeRST (a voltage-sensitive dye) for 30 minutes, washed twice with PBS, and imaged using a Leica SP8 Confocal microscope. Fluorescence Lifetime Imaging Microscopy (FLIM) was used, exciting BeRST at 658 nm and collecting emissions from 681–800 nm. Images were processed by fitting the signal with a biexponential decay curve. Resulting FLIM images were exported as .TIF files and processed in ImageJ for single-cell segmentation using Otsu thresholding. Mean lifetime values per cell were extracted and analyzed using GraphPad Prism or RStudio.

Spatial autocorrelation imaging and analysis (Moran's I)

To evaluate spatial autocorrelation in V_{mem}, cells were stained with either the voltage-sensitive dye VF2.1 or its voltage-insensitive control VF2.0. VF2.0 lacks the aniline donor group necessary for voltage sensitivity and served as a control for non-V_{mem}-related spatial patterning. Higher concentrations of VF2.0 led to quenching artifacts; therefore, 50 nM was used for all experiments. Cells at various timepoints were seeded into 96-well plates 24 hours before imaging. They were stained with 50 nM VF2.1 and 1 μM Hoechst 33342 for 30 minutes at 37 °C, then imaged using a Leica SP8 Confocal microscope equipped with a 25× air objective. Segmentation masks were created by applying Otsu thresholding to intensity images, and background pixels were set to zero. A custom Python script scanned each image using a 15 × 15 pixel region of interest (ROI), saving X and Y coordinates and FLIM lifetime values for non-background pixels. Results were saved as .csv files for downstream spatial analysis. An elbow method was used to determine the optimal value of k (number of nearest neighbors), yielding k = 3. Subsamples of 1000 cells were taken, and Moran's I values were averaged over 10 iterations to account for variability in cell number.

Chromatin Condensation Parameter (CCP) quantification

To assess chromatin compaction, CCP was computed from Hoechst-stained nuclear images. Cells were stained with 1 μM Hoechst 33342 for 30 minutes at 37 °C and 5% CO_2, washed twice with PBS, and imaged immediately using the ImageXpress® Confocal HT.ai system (10× Plan Apo 0.45 NA air objective, single-plane acquisition). Image processing included: (1) Gaussian blur ($\sigma = 2$) to reduce noise, (2) Sobel edge detection to enhance nuclear structure, (3) Otsu thresholding to binarize the edge map, (4) Skeletonization to reduce chromatin edges to linear forms and reduce processing time. Only signals within nuclear boundaries were retained. The number of 'on' (skeletonized) pixels was divided by the nuclear area to generate the CCP value for each nucleus.

Senescence-associated β-galactosidase (SA-β-Gal) assay

Cells were seeded into 96-well plates 48 hours before assay. SA-β-Gal staining was performed using the Cell Signaling Technologies kit (Cat# 9860), following manufacturer instructions. Briefly, cells were fixed, washed, stained, sealed with parafilm, and incubated for 24 hours in a dry (non-CO_2) incubator. Hoechst 33342 was then used for nuclear counterstaining. Images were acquired using an EVOS M7000 microscope and processed in ImageJ following Krzystyniak et al.[130]: color thresholding to segment stained cells, inversion of the signal, and measurement of integrated density. This value was divided by the number of nuclei to yield the integrated SA-β-Gal density per cell.

RT-qPCR

Total RNA was isolated with the Qiagen RNeasy Mini Kit (Cat# 74104). 200 ng of RNA was reverse transcribed using iScript™ cDNA Synthesis Kit (Bio-Rad, Cat# 1725035). qPCR was performed using PowerUp™ SYBR™ Green Master Mix (Thermo Fisher, Cat# A25777).

The following primers were used: $p16^{INK4A}$: Fwd – CTCGTGCTGATGCTACTGAGGA; Rev – GGTCGGCGCAGTTGGGCTCC; - IL1-α: Fwd – TGTATGTGACTGCCCAAGATGAAG; Rev – AGAGGAGGTTGGTCTCACTACC; - IL6: Fwd – AGACAGCCACTCACCTCTTCAG; Rev – TTCTGCCAGTGCCTCTTTGCTG; - IL8: Fwd – GAGAGTGATTGAGAGTGGACCAC; Rev – CACAACCCTCTGCACCCAGTTT; - Lambda DNA (standard): Fwd – CTGCTGGCCGGAACTAATGAATTTATTGGT; Rev – ATGCCACGATGCCTCATCACTGTTG. Thermal cycling conditions were: 50 °C for 2 min for activation, 95 °C for 10 min for denaturation, followed by 40 cycles of 95 °C for 15 s and 60 °C for 1 min. A melt curve was performed with 95 °C for 15 s, 60 °C for 15 s, and 95 °C for 15 s. Quantification was done using the Linear Regression of Efficiency method.[129] 100 fg of lambda DNA was used as an internal reference standard for all transcripts.

QUANTIFICATION AND STATISTICAL ANALYSIS

All statistical analyses were performed using RStudio or GraphPad Prism. Specific statistical tests and exact *n* values are reported in the figure legends and results section. Moran's I spatial autocorrelation was calculated using custom R scripts. For each experimental condition, FLIM lifetime data were analyzed in biological replicates ($n > 3$). Each replicate included >1000 cells. Optimal k was determined via elbow method (k = 3), and analysis was repeated across 10 random subsampling to ensure robustness.

Chromatin Condensation Parameter (CCP) values were measured per nucleus and averaged across biological replicates ($n > 3$). Distributions were assessed for normality using the Shapiro–Wilk test. Group comparisons were made using one-way ANOVA or Kruskal–Wallis test, depending on distribution.

SA-β-Gal activity was normalized to nuclei count and quantified per well. Data from independent replicates ($n > 3$) per condition were compared using unpaired two-tailed t-tests or Mann–Whitney U-tests as appropriate.

RT-qPCR results were obtained from three independent biological replicates. Expression levels were calculated using the Linear Regression of Efficiency method and normalized against 100 fg of lambda DNA. Group differences were assessed by one-way ANOVA followed by Dunnett's post-hoc test.

All data are reported as mean ± standard error of the difference (SED) unless otherwise noted. A significance threshold of $p < 0.05$ was used throughout. No blinding or randomization was applied. No data were excluded except in the case of technical imaging errors.